This document is downloaded from DR-NTU (https://dr.ntu.edu.sg)
Nanyang Technological University, Singapore.

Ultrathin 2D photocatalysts : electronic-structure tailoring, hybridization, and applications

Di, Jun; Xiong, Jun; Li, Huaming; Liu, Zheng

2017

Di, J., Xiong, J., Li, H., & Liu, Z. (2018). Ultrathin 2D photocatalysts : electronic-structure tailoring, hybridization, and applications. Advanced Materials, 30(1), 1704548-. doi:10.1002/adma.201704548.

https://hdl.handle.net/10356/84053

https://doi.org/10.1002/adma.201704548

This is the peer reviewed version of the following article: Di, J., Xiong, J., Li, H., & Liu, Z. (2018). Ultrathin 2D photocatalysts : electronic-structure tailoring, hybridization, and applications. Advanced Materials, 30(1), 1704548-, which has been published in final form at https://doi.org/10.1002/adma.201704548. This article may be used for non-commercial purposes in accordance with Wiley Terms and Conditions for Use of Self-Archived Versions.

Downloaded on 27 Aug 2022 02:15:09 SGT

WILEY-VCH

DOI: 10.1002/ ((please add manuscript number))
Article type: Review

Ultrathin Two-dimensional Photocatalysts: Electronic Structure Tailoring, Hybridization and Applications

Jun Di[‡], Jun Xiong[‡], Huaming Li[*], Zheng Liu[*]

((Optional Dedication))

Dr J. Di, J. Xiong, Prof. H. M. Li
School of Chemistry and Chemical Engineering, Institute for Energy Research, Jiangsu University, 301 Xuefu Road, Zhenjiang, 212013, P. R. China
E-mail: lhm@ujs.edu.cn
Dr. J. Di, Prof. Z. Liu
Center for Programmable Materials, School of Materials Science & Engineering, Nanyang Technological University, Singapore 639798, Singapore
E-mail: z.liu@ntu.edu.sg
Dr. J. Xiong
School of Mechanical and Aerospace Engineering, Nanyang Technological University, Singapore 639798, Singapore

Keywords: ultrathin, two-dimensional, photocatalytic, electronic structure tailoring, hybridization

Abstract: As a sustainable technology, semiconductor photocatalysis have aroused considerable interests in the past several decades owing to the potential to relieve or resolve energy and environmental pollution issues. By virtue of the unique structural and electronic properties, the emerging ultrathin 2D materials with appropriate band structure show enormous potential to achieve the efficient photocatalytic performance. Here, we review the state-of-art progress on the ultrathin 2D photocatalysts and present a critical appraisal of the classification, controllable synthesis and formation mechanism of ultrathin 2D photocatalysts. Then, different strategies to tailor the electronic structure of ultrathin 2D photocatalysts are summarized, including component tuning, thickness tuning, doping and defect engineering. Hybridizations with the introduction of foreign component and maintaining the ultrathin 2D structure are presented to further boost the photocatalytic performance, such as quantum dot/2D materials, single atom/2D materials, molecular/2D materials, and 2D-2D stacking materials. More important, the advancement of versatile photocatalytic

applications of ultrathin 2D photocatalysts in the fields of water oxidation, hydrogen evolution, CO_2 reduction, nitrogen fixation, organic syntheses, and pollutants removal will be discussed. Finally, we also present the future opportunities and challenges in the ultrathin 2D photocatalysts to bring about new opportunities for future research in the field of photocatalysis.

1. Introduction

Ultrathin two-dimensional (2D) materials, with the thickness is only single- or few-atoms thick (typically less than 5 nm), display unusual mechanical, optical, and electronic properties, have been attracting a great deal of research interest for diverse applications such as field effect transistors, optoelectronic devices, catalysis, energy storage and conversion.[1-5] Benefiting from the features of atomic thickness, large specific surface area, intrinsic quantum confined electrons and high ratio of surface atoms to entire atoms, the ultrathin 2D materials exhibit unique physicochemical properties, such as planar conductivity, electronic anisotropy, tunable energy band structure, and high surface activity.[6, 7] When the thickness of bulk materials are reduced to atomically level, the local atomic structures will suffer from obvious distinctions including coordination number, bond angle, bond length, and disorder degree of the surface atoms and may even result in the formation of numerous surface defects. As a consequence, the ultrathin 2D materials can not only display improved inherent properties of the bulk materials but also give birth to new properties that the corresponding bulk materials do not possess.[8, 9]

Semiconductor photocatalysis has attracted massive research interest since it has been regarded as one of the most promising solutions to deal with the energy shortage and environmental pollution issues.[10-14] With the solar light as the external driving force, the semiconductor could split water into hydrogen and oxygen, reduce the CO_2 to chemicals and valuable fuel as well as completely eliminating pollutants.[15-18] Generally, the major critical steps in the photocatalytic process can be classified as light absorption, charge separation and migration as well as surface redox reactions.

Under the irradiation, the photocatalysts can absorb the solar light and been excited to produce electron-hole pairs when the photon energy equal to or higher the band gap, leaving the electrons in the conduction band (CB) and holes in the valence band (VB), respectively. Subsequently, the photogenerated electrons and holes will diffuse to the materials surface and further migrate to the surface active sites before involving in the surface reactions. During this process, the recombination of charge carriers will happen and the crystal structure, crystallinity, particle size and surface atomic structure etc. will strongly affect the separation efficiency. Finally, the target molecule will be adsorbed on the materials surface, undergo charge injection process and desorption to form the ultimate products.[19] Up to now, hundreds of semiconductor materials are available for different photocatalytic applications with the help of various tuning ranging from composition, crystal structure and electronic structure. Although significant achievements have been obtained in optimizing the photocatalytic behavior, most photocatalysts still suffer from relative low photocatalytic efficiency which is far below the requirements for possible practical applications. The key issue to achieve the outstanding photocatalytic performance rely on the rational design of high-efficiency photocatalysts. Considering the numerous features and advantages, the emerging ultrathin 2D materials with appropriate energy band structure can awaken the new prospect. This ultrathin 2D configuration can supply huge specific surface area and a large fraction of low-coordinated surface atoms to harvest more ultraviolet-visible light, while the photon absorption in bulk materials or nanosized particles often being limited by light transmittance and reflection at the grain boundaries.[20] Moreover, owing to the atomic thickness greatly shorten the migration distance, the charge carriers generated in the 2D materials interior will be faster to migrate to the surface than the bulk materials. This will greatly reduce the recombination possibility of photogenerated charge carrier and favor the photocatalytic process. At last, with respect to the surface redox reactions, the unique 2D structure with the high ratio of surface atoms to overall atoms can render more active sites to accelerate reaction progress. In addition, the atomic-escape energy becomes relatively small when

the thickness reduced to atomic scale and thus more surface defects will appear. The existence of surface defects contribute to better target molecule adsorption to build strong interplay, easier charge transfer and superior activation process. Profiting from these features, the photocatalysts with ultrathin 2D structure can display enormous prospect and lots of related studies have been carried out.[21-23] It is highly desirable and urgent to present a comprehensive review on this subject to promote the further developments in this emerging area.

In this review, we thoroughly summarize recent advances in the area of ultrathin 2D nanostructured semiconductors for diverse photocatalytic applications. The quite disperse literatures regarding ultrathin 2D photocatalysts have been classified as metal oxides, metal composite oxides, metal hydroxides, metal chalcogenides, bismuth-based materials and metal-free photocatalysts. Then, the strategies to tailor the electronic structure of ultrathin 2D photocatalysts has been summarized, namely component tuning, thickness tuning, doping, defect engineering. The further hybridization with the maintaining of ultrathin 2D feature has been presented, including quantum dot/2D materials, single atom/2D materials, molecular/2D materials, and 2D-2D stacking materials. This review will further introduce different photocatalytic applications of ultrathin 2D materials in the fields of water oxidation, hydrogen evolution, CO_2 reduction, nitrogen fixation, organic syntheses, and pollutants removal. Finally, the challenges and key issues that need to be addressed during the future researches will be proposed.

2. Two-Dimensional Photocatalysts

As ideal candidates for photocatalysis, the mainly studied 2D photocatalysts can be classified as several types, including metal oxides, metal composite oxides, metal hydroxides, metal chalcogenides, bismuth-based materials and metal-free photocatalysts.

2.1. Metal Oxides

Metal oxides are the most widely studied photocatalysts by far. Constructing ultrathin 2D metal oxides has been regarded as an effective approach to optimize the specific surface area, charge migration and thus achieve an efficient photocatalytic behavior. Up to now, several metal oxides with ultrathin 2D structures have been controlled prepared and applied to photocatalysis applications, such as TiO_2, ZnO, WO_3, Fe_2O_3, Cu_2O, SnO, CeO_2, In_2O_3, HNb_3O_8 and so on.[24-35] Since the intrinsic non-layered structured feature, some ultrathin 2D metal oxides are difficult to be synthesized via the simply direct ultrasonic exfoliation method from these bulk counterpart. Therefore, several alternative routes have been selected for the controlling preparation of ultrathin 2D metal oxides. For example, a lamellar inorganic-organic hybrid intermediate strategy is proposed to prepare the TiO_2 ultrathin nanosheets.[24] By using Ti-isopropoxide as Ti source, 2-phenyl ethanol as solvent and octylamine as capping reagent, the lamellar TiO_2-octylamine hybrid precursors can be obtained through a solvothermal treatment (**Figure 1**). After ultrasound exfoliation in formamide, the product is washed to remove octylamine and acquire the clean TiO_2 ultrathin nanosheets. According to the AFM result, the average thickness of the TiO_2 is determined to be 1.66 nm, suggesting the successful preparation of TiO_2 ultrathin nanosheets. The critical point for this synthetic strategy rely on the construction of hybrid intermediate. Many other types of metal oxides nanosheets such as Cu_2O,[31] In_2O_3[34] can also be prepared via the similar paths. Profiting from the ultrathin thickness, the increased density of states (DOS) near the Fermi level as well as increased charge density on the surface for ultrathin TiO_2 nanosheets can be acquired. As such, the ultrathin TiO_2 nanosheets display faster carriers transport and thus achieve a 450 times higher photocatalytic activity than bulk TiO_2 towards CO_2 reduction for formate formation. In addition, single-crystalline WO_3 nanosheets can be achieved by exfoliation from $Bi_2W_2O_9$.[29] Owing to the layered structure of $Bi_2W_2O_9$ consists of $[W_2O_7]^{2-}$ and $[Bi_2O_2]^{2+}$ layers, the WO_3 layers can be achieved by selective etching of $[Bi_2O_2]^{2+}$ layers by hydrochloric acid treatment and the WO_3 layers will be stabilized in the presence of tetrabutylammonium hydroxide surfactant. After the exfoliation, the WO_3 nanosheets shows

increased band gap relative to bulk WO_3 due to the quantum confinement effect. Apart from exfoliation process, the directly preparation process of metal oxides ultrathin nanosheets can also be achieved via wet-chemical method. Through a surfactant self-assembly strategy with polyethylene oxide-polypropylene oxide-polyethylene oxide as surfactant and ethylene glycol as co-surfactant, various metal oxides with ultrathin thickness can be prepared, such as TiO_2, ZnO, Co_3O_4, WO_3, Fe_3O_4 and MnO_2.[36]

2.2 Metal Composite Oxides

Similar to the metal oxides, the metal composite oxides can also show superiority towards photocatalysis and several metal composite oxides have been controlled prepared with ultrathin thickness.[37, 38] According to the acid-base reaction and ion intercalation assisted exfoliation process, the $HNbWO_6$ ultrathin nanosheet can be obtained by dispersing the layered $HNbWO_6{\cdot}1.5H_2O$ into triethanolamine aqueous solution.[39] AFM result suggests the thickness of the $HNbWO_6$ ultrathin nanosheet is between 1.8 and 2.0 nm, which agree with value of monolayer. The as-prepared ultrathin $HNbWO_6$ nanosheet suspensions can display efficient activity for photocatalytic hydrogen evolution with an optimal rate of 158.9 μmol h^{-1}. Moreover, ion exchange strategy by using ultrathin precursor can be employed for synthesizing the metal composite oxides. For example, the ultrathin $SnNb_2O_6$ nanosheets can be acquired by using $K_4Nb_6O_{17}$ nanosheets and $SnCl_2$ as the precursors.[40] By virtue of the ultrathin thickness of $K_4Nb_6O_{17}$, the thickness can be maintained in $SnNb_2O_6$ with a thickness about 3 nm, as demonstrated by AFM analysis. Compared to the bulk $SnNb_2O_6$, ultrathin $SnNb_2O_6$ nanosheets has increased band gap and more negative CB potential, meaning the stronger reduction ability for photocatalytic hydrogen evolution. Moreover, the charge transfer efficiency in the ultrathin $SnNb_2O_6$ nanosheets is also improved due to the ultrathin thickness. As a result, further study indicates that the excellent visible light hydrogen evolution activity can be obtained over ultrathin $SnNb_2O_6$ nanosheets, roughly 14 times higher than bulk $SnNb_2O_6$.

2.3 Metal Hydroxides

Ultrathin metal hydroxides have been increasingly considered as an important category in 2D nanomaterials, which show exciting perspectives in many fields such as catalysis, energy storage and conversion.[41] Owing the ease of regulation for the cations, the desired band gap can be achieved in metal hydroxides by incorporating particular photoactive metal cations.[42] Therefore, metal hydroxides with ultrathin 2D structure display tremendous potential towards photocatalytic applications. For instance, ZnAl-LDH ultrathin nanosheets can be synthesized through a reverse micelle method and serve as photocatalyst for converting CO_2 to CO.[43] By using sodium dodecylsulfate as surfactant, 1-butanol as co-surfactant, a transparent and stable reverse emulsion system can be formed in isooctane/water mixed solution. After the Zn and Al sources are added into the mixed solution, urea is employed to create alkaline condition and prepare the ZnAl-LDH with ultrathin structure. The thickness is determined to be ca. 2.7 nm from the standing sheets in TEM image and corresponding to 2 LDH layers thick. Benefiting from the ultrathin thickness, the oxygen vacancies (V_o) are created in ZnAl-LDH ultrathin nanosheets, and resulting in the formation of Zn^+-V_o complexes. According to density-functional-theory (DFT) calculations, new defect level in which hybridized with contribution from both occupied Zn 4s orbitals and O 2p orbitals appears in the band gap of ZnAl-LDH ultrathin nanosheets relative to bulk ZnAl-LDH. The Zn^+-V_o complexes can serve as electron trapping sites for CO_2 photoreduction. As a result, a significantly increased photocatalytic activity for CO_2 reduction can be acquired for ZnAl-LDH ultrathin nanosheets relative to bulk ZnAl-LDH. Apart from ZnAl LDH, many other metal hydroxides with ultrathin thickness, such as CoOOH,[44] NiTi LDH,[45] ZnTi LDH,[46] also show outstanding activity for different photocatalytic applications.

2.4 Metal Chalcogenides

Owing to the unique electronic structure, metal chalcogenides can usually show relatively wide light absorption region, which have been considered to be a class of promising materials towards photocatlytic applications. Recently, numerous ultrathin 2D metal chalcogenides have been

controlled prepared and display outstanding photocatlytic performance, including CdS, MoS_2, SnS, SnS_2, In_2S_3, $ZnIn_2S_4$, SnSe, and ZnSe.[47-55] The synthetic methods of these ultrathin 2D metal chalcogenides mainly focus on exfoliation thanks to the intrinsic layered structures. Take the hexagonal SnS_2 for example, the SnS_2 single-layers can be acquired by refluxing the bulk SnS_2 in formamide to break the interlayer van der Waals interactions.[51] The nearly transparent feature of SnS_2 nanosheets in TEM image reveals the ultrathin thickness and the thickness is determined to be 0.61 nm through the AFM, in good agreement with the single-layered SnS_2 slab along the [001] direction. Due to the single layer configuration, the electronic structure of SnS_2 single-layers undergo distinct variation, with increased band gap, higher DOS at the VB edge, and faster interfacial charge transfer. As a result, the SnS_2 single-layers delivery a remarkably improved photocatalytic water-splitting performance (70 times improvement) than bulk SnS_2 under visible light.

2.5 Bismuth-based Materials

Recent years, the bismuth-based materials have been widely studied in photocatalysis field, owing to the Bi 6s in Bi(III) can hybridize with O 2p orbitals to create a new preferable hybridized VB and the band gap of bismuth-based materials can be narrowed for visible light absorption. To further promote the photocatalytic behavior, several Bi-based materials with controlled ultrathin thickness have been prepared, such as Bi_2WO_6,[56-58] Bi_2MoO_6,[59] $BiVO_4$,[60] Bi_2SiO_5,[61] $(BiO)_2CO_3$,[56] Bi_3NbO_7,[62] and BiOX (X = Cl, Br, I).[63-68] For example, the monolayered Bi_2WO_6 nanosheets has been synthesized via a surfactant cetyltrimethylammonium bromide (CTAB) assisted hydrothermal method.[56] During the formation process, the Br^- ions from the CTAB can be strongly adsorbed on the surface of Bi_2WO_6 monolayers and the formed Coulomb repulsion forces can hinder the stacking of Bi_2WO_6 monolayers. Moreover, the hydrophobic long-chain cationic CTA^+ on the surface of Bi_2WO_6 can supply extra surface repulsion to prevent the further crystal growth along the c axis. As a consequence, the monolayer Bi_2WO_6 slab (0.8 nm thickness) with the $[BiO]^+$-$[WO_4]^{2-}$-$[BiO]^+$ sandwich substructure can be obtained, as testified by AFM images (**Figure 2**). The abundant

coordinatively unsaturated Bi atoms can be exposed on the monolayer Bi_2WO_6 surface and serve as active sites. Under light irradiation, the holes are generated in the $[BiO]^+$ while the electrons in the $[WO_4]^{2-}$. Similar to the heterojunction interface, the sandwich $[BiO]^+$-$[WO_4]^{2-}$-$[BiO]^+$ substructure allows the effective space charge separation in the interface. Benefiting from these features, the monolayer Bi_2WO_6 can display significantly improved photocatalytic activity towards pollutant removal under visible light. Furthermore, the as-prepared monolayer Bi_2WO_6 can show hydrogen evolution activity under visible light although the Bi_2WO_6 nanocrystal indeed hold no hydrogen evolution activity.

By changing the surfactant type to polyvinylpyrrolidone (PVP), the BiOCl ultrathin nanosheets can be achieved via a solvothermal treatment.[63] The thickness of the BiOCl nanoplates (ca. 30 nm) can be decreased to 2.7 nm when the PVP is employed as capping agent, as demonstrated by the AFM image. Owing to the polyvinyl skeleton, the PVP can prevent the further growth of BiOCl nanocrystal by creating the passivation layer around BiOCl cores through the strong interaction with Bi^{3+} and O, N atoms of the pyrrolidon ring. It will suppress the agglomeration of BiOCl nanocrystal along c-axis through the nature of the repulsive forces among the polyvinyl groups. As a result, the BiOCl nanosheets with ultrathin thickness can be controlled prepared via this PVP assisted solvothermal strategy, and this route can be further utilized for the synthesis of BiOBr and BiOI with ultrathin 2D configuration.[64, 66] The achieved ultrathin thickness endow the BiOCl ultrathin nanosheets with upshifted CB and VB potentials as well as reduced band gap relative to BiOCl nanoplates. As such, effectively separation of the photoinduced electron-hole pairs can be acquired and leading to an increased photocatalytic activity for pollutant removal.

2.6 Metal-free Photocatalysts

Apart from metal-contain semiconductors, the metal-free materials can also be developed as photocatalysts. The graphitic carbon nitride (g-C_3N_4) is the most representative promising metal-free photocatalyst. Benefiting from the unique energy band structure, g-C_3N_4 is active to various

photocatalytic applications such as hydrogen evolution, CO_2 reduction, pollutant removal, disinfection and so on. Owing to the graphite-like layered structure with strong C-N covalent bonding in the in-plane direction and interlayer weak van der Waals forces, the bulk g-C_3N_4 is liable to be exfoliated to achieve the few-layer or even single-layer structure. There are mainly two approaches for the exfoliation of g-C_3N_4, namely thermal oxidation exfoliation and ultrasonication-assisted liquid exfoliation. Considering the hydrogen-bond cohered strands of polymeric melon units in the layers are not stable enough against oxidation, Liu et al. developed a thermal oxidation exfoliation route to prepare g-C_3N_4 ultrathin nanosheets.[69] The thickness of bulk g-C_3N_4 can be gradually decreased with the extended times via a layer-by-layer etching process (**Figure 3**). After the thermal oxidation for 120 min, the g-C_3N_4 nanosheets with thickness about 2 nm can be acquired. Due to the quantum confinement effect, the enhanced bandgap, promoted electron migration rate along the in-plane direction can be achieved, and thus responsible for the 5.4 times improved hydrogen evolution activity compared with bulk counterpart. Inspired by this route, several further researches are performed to prepare g-C_3N_4 ultrathin nanosheets via the modified methods.[70-73]

The ultrasonication-assisted liquid exfoliation has been regarded as another effective method to achieve the g-C_3N_4 ultrathin nanosheets due to the intrinsically layered structure. During the exfoliation process, the efficiency is strongly affected by the surface energies of the solvent molecules. When the surface energies of the solvent and bulk materials match each other, the exfoliation efficiency will be very high. On the basis of the calculation, the surface energy of g-C_3N_4 is about 115 mJ m^{-2}, in good agreement with that of H_2O (about 102 mJ m^{-2}). Thereby, the H_2O is employed for the liquid exfoliation of g-C_3N_4, and the exfoliated nanosheets with thickness about 2.5 nm can be obtained.[74] According to the similar principle, Ajayan et al. demonstrated the successful exfoliation of g-C_3N_4 by using isopropanol.[75] The as-prepared g-C_3N_4 nanosheets shows uniform thickness of about 2 nm. Profiting from the ultrathin thickness, the g-C_3N_4 nanosheets display increased band gap and enhanced charge migration rate compared with bulk g-C_3N_4, and thus result

in the 9.3 times higher photocatalytic hydrogen evolution rate. To further promote the exfoliation, several other solvents have also been explored to prepare the ultrathin g-C_3N_4 and acquire the improved photocatalytic performance.[76, 77]

Apart from g-C_3N_4, other metal-free materials can also serve as photocatalysts towards various applications.[78] For instance, the silicon ultrathin nanosheets can be controlled synthesized through molten-salt-induced exfoliation and chemical reduction of natural clay.[79] The silicon ultrathin nanosheets (~5 nm thickness) can display outstanding hydrogen evolution behavior from a water-methanol mixture. Further study demonstrated that the efficient water splitting can be acquired over silicon ultrathin nanosheets without the addition of any cocatalyst or sacrificial agent.[80] Unfortunately, the silicon ultrathin nanosheets suffer from serious activity deterioration with the extended time. How to adopt appropriate strategy to improve the stability may be the heart of the water splitting over silicon ultrathin nanosheets.

3. Electronic Structure Tailoring

Through the tailoring of electronic structure, the properties of ultrathin 2D materials will suffer from distinct variation, providing opportunities to optimize or even induce new photocatalytic activity for the material. There are various strategies to tailor the electronic structure of ultrathin 2D materials, including component tuning, thickness tuning, doping and defect engineering.

3.1. Component Tuning

For photocatalytic applications, the component of a semiconductor determines the band structure. Owing to reactivity of photogenerated electrons and holes towards corresponding surface redox reactions is generally determined by the band edge potentials, thus the component of the semiconductor show greatly impart on the photocatalytic behaviors. Especially for the ultrathin 2D materials, the electronic structure is strongly depends on the corresponding component. Maeda et al. prepared the $HCa_{2-x}Sr_xNb_3O_{10}$ and $HCa_2Nb_{3-y}Ta_yO_{10}$ nanosheets with controlled energy band structure through exchanging interlayer K^+ ions with protons in layered $KCa_{2-x}Sr_xNb_3O_{10}$ and

$KCa_2Nb_{3-y}Ta_yO_{10}$ and then further suffer from exfoliation.[37] Through the gradual tuning in the atomic component of the nanosheets, the optical absorption of the samples is greatly affected (**Figure 4**). In detail, onset absorption edge of $HCa_{2-x}Sr_xNb_3O_{10}$ shows obvious red-shift with the Sr content improved, accompanied by the band gap energy decreased from 3.59 (x = 0) to 3.40 eV (x = 2). In addition, the blue-shift of the onset absorption edge can be observed for the $KCa_2Nb_{3-y}Ta_yO_{10}$ with the higher Ta contents. The replacement of Nb^{5+} by Ta^{5+} ions will lead to a more negative CB potential, which is responsible for the blue-shift of the onset absorption edge. Thereby, the tunable light absorption behavior can be acquired by adjusting the component and further shows significant impact on the photocatalytic hydrogen evolution performance. By employing the similar strategy, the energy band structure of ternary sulfides $H_{2x}Zn_{1-x}In_2S_4$ can be effective tuned with the $ZnIn_2S_4$ show the optimal photocatalytic hydrogen evolution rate.[54]

Another important case is the adjusting of halogen: oxygen ratio in bismuth oxyhalide to tune the electronic structures. According to DFT calculation, the VB top of bismuth oxyhalide is primarily composed of hybrid orbitals of O 2p orbitals and X np (n = 3, 4, and 5 for X = Cl, Br, and I) orbitals, whereas the CB bottom is mainly consisted of Bi 6p orbitals. Through the tuning of O, X component, the band gap and band edge potentials can be effective tailored. Up to now, several bismuth oxyhalide ultrathin nanosheets with tuned O, X component has been controlled prepared, such as $Bi_{12}O_{17}Cl_2$,[81] $Bi_4O_5Br_2$,[82, 83] $Bi_4O_5I_2$[84, 85] and so on. Generally, with the decrease of Cl or Br content, the obtained materials will show narrowed band gap compared with corresponding BiOCl or BiOBr and the decrease of I content will result in the increase of band gap relative to BiOI. Profiting from the energy band structure diversity, the tuned bismuth oxyhalide ultrathin nanosheets can show superiority towards various photocatalytic applications.

3.2. Thickness Tuning

The thickness of the semiconductor is a significant influence factor towards the electronic structure tailoring and photocatalytic behavior optimizing. Owing to the well-known quantum

confinement effect, the band gap of the semiconductor will undergo broadening when the thickness of materials gradually reduced. In addition, surface effect will aggravated when the thickness reduced to atomically-thin. The electronic density of states can be strongly improved at the surface of ultrathin 2D materials compared with that in the interior of bulk materials. These features will show important effect on the photocatalytic performance of the ultrathin 2D materials.

Through the thermal oxidation etching treatment, the C_3N_4 ultrathin nanosheets with the thickness about 2 nm can be prepared.[69] After the thickness decreased to atomically-thin, the electronic structure of C_3N_4 suffer from significant difference. Owing to the quantum confinement effect, the band gap can increase from 2.77 eV for bulk C_3N_4 to 2.97 eV for the ultrathin nanosheets. At the same time, the reduced thickness ensures an enhanced electron transport ability along the in-plane direction, and improved lifetime of photogenerated charge carriers. Further study found that the CB edge of the C_3N_4 ultrathin nanosheets will show upshift relative to that of bulk counterpart.[73] As a result, the photogenerated electrons will hold stronger reduction ability and beneficial to the photocatalytic hydrogen evolution behavior. Apart from C_3N_4, the electronic structure tailoring can also be acquired within other semiconductors by thickness tuning. By reduce the thickness of bulk $SnNb_2O_6$ to 50 and 3 nm, the corresponding band gap can increase from 2.30 to 2.35 and 2.43 eV, respectively, accompanied with the upshifting of CB edge.[40] These results suggest the thickness tuning is effective to adjust the energy band structure of semiconductors.

Additionally, when the thickness of bulk materials gradually decreased to atomically-thin or even single layer, the ratio of the exposed surface atoms to the entire atoms will be sharply increased. Since the absence of neighbouring atoms, there will form abundant coordination-unsaturated surface atoms with dangling bonds. These surface atoms are inclined to bonding with other atoms to achieve stabilization. Thereby, the abundant surface atoms can display high surface energy and chemical activity. Freestanding SnS and SnSe nanosheets with all-surface-atom exposure can be obtained by exfoliating the bulk SnS or SnSe in a mixed solvent of ethanol and water.[50] Take the SnS for

instance, the large-area sheet-like morphology with lateral size of about 500 nm and nearly transparent feature can be observed from TEM analysis, revealing the ultrathin thickness of the as-prepared sample (**Figure 5**). The average height of the SnSe nanosheet can be determined to be 0.57 nm by AFM analysis, agree with the thickness of half of a unit cell. After the successful exfoliating to single layer, the calculated band structures suggest the variation from an indirect semiconductor for bulk SnS to a direct semiconductor for SnS single layers. Compared to the bulk SnSe, the improved state density can be obtained at the VB edge of SnS single layer, which can enable the SnS single layer with increased carrier transport efficiency. Benefiting from the single layer structure, the SnS single layers display increased photoabsorption efficiency and charge separation efficiency and then promote the water splitting behavior.

3.3. Doping

The suitable doping has been regarded as an effective strategy for tailoring the physicochemical properties of materials. The deliberate engineering foreign metal or nonmetal element into the semiconductor lattice offer the opportunity to tune the electronic or surface structures of the host material for boosting the photocatalytic behavior. The types, concentrations, and the distribution of the dopants will all have significant influence on the properties of the host semiconductors. Benefiting from the atomically-thin feature, the doping may be a more feasible strategy to affect the properties of ultrathin 2D materials. Generally, the doping always occurs on the shallow surface of the bulk materials owing to the absence of atom permeation gallery, which will show less influence on their entire behavior. With respect to ultrathin 2D materials, the atomically thickness allow the effective doping of dopants, only requiring tiny diffusion deepness. Therefore, it is highly desirable to engineering heteroatom into the ultrathin 2D materials and construct high-efficiency systems.

3.3.1. Metal Doping

Through the incorporation of metal ions into the crystal lattice, the impurity levels will be formed during the forbidden band of semiconductors. The redshift of onset light absorption edge can

be usually observed, which is ascribed to the transition between the impurity levels to CB or VB. Generally, the highly efficient doped photocatalysts primarily rely on the doping tuning of metal ions, which should satisfy to the following criteria. (1) The electrons and holes can be trapped by dopant, and further ensure the effective local separation. (2) The captured electron and hole can be released and transfer to the surface effectively. Xie's group doped Co ions into the In_2S_3 ultrathin nanosheets for optimizing the photocatalytic water splitting performance.[52] By virtue of a lamellar inorganic-organic hybrid intermediate strategy, the Co doped In_2S_3 nanosheets (0.59 nm thickness) with only three atomic layer thick can be controlled prepared (**Figure 6**). The electronic structure of perfect In_2S_3 with three atomic layers and Co doped In_2S_3 is first determined through the DFT calculations. According to calculated result, the presence of Co dopant ensure the In_2S_3 ultrathin nanosheets with obviously increased DOS at CB minimum compared with the perfect In_2S_3 ultrathin nanosheets. In addition, the Co ions doping endow the Co-doped In_2S_3 materials with several new energy levels, which may derived from the splitting of Co 3d states. Under light irradiation, the electrons can be easily excited via the d→d internal transition of Co ions in tetrahedral coordination, enabling the formation of more photogenerated electron-hole pairs. This result is verified by the light absorption difference of In_2S_3 ultrathin nanosheets and Co-doped In_2S_3 in the UV/Vis diffuse reflectance spectra. The significantly improved light absorption can be observed from 600 to 2000 nm, which is assigned to the formation of dopant energy levels of Co. Benefiting from the Co ions doping, the photogenerated charge separation efficiency is greatly improved with circa 25-fold increased average recovery lifetime, as certified by ultrafast transient absorption spectroscopy. As a result, the Co ions doping allow a 10 times improved photocatalytic activity towards water splitting than perfect In_2S_3 ultrathin nanosheets.

Apart from Co, other metal elements have also been employed for doping to tune the electronic structure of ultrathin 2D host photocatalyst, such as Rh, Cr, Cu, Pt, Fe and so on.[86-89] For instance, the Fe ions are doped into BiOCl ultrathin nanosheets and can extend the light absorption range from

ultraviolet light to visible light.[68] The photocatalytic activity towards pollutant removal and hydrogen evolution can thus be promoted. These result undoubtedly demonstrate that the metal element doping is an effective tool to tailor the electronic structure of ultrathin 2D photocatalysts and can further boost the photocatalytic behavior.

3.3.2. Non-metal doping

With respect to the non-metal elements doping, two dominating hypotheses have been put forward to tune the electronic structure and further affect photocatalytic behavior. One is the dopants can build localized states among the forbidden band and another is the merging of the occupied dopant states with the upper edge of the VB and upshift the VB maximum. These two different mechanisms mainly stem from the different doping form, in which the surface doping will lead to the formation of localized states and the homogeneous doping will elevate VB maximum.[90] Owing to the mobility of holes in the localized states is sluggish and then limit the photocatalytic performance, thereby performing homogeneous distribution of the dopant to upshift the VB maximum and promote the hole migration may be more preferable. The atomically thickness of ultrathin 2D materials will facilitate the homogeneous doping due to the wee doping depth is required.[91, 92] For instance, by engineering oxygen atoms into the $ZnIn_2S_4$ ultrathin nanosheets to substitute the lattice sulfur atoms, the electronic structure will suffer from distinct difference from the pristine $ZnIn_2S_4$ ultrathin nanosheets.[53] On the basis of the DFT calculations, the oxygen doping can effective strengthen the DOS at VB maximum compared with pure $ZnIn_2S_4$, revealing the formation of improved charge density around the VBM. Both of the CB edge and VB edge in O-doped $ZnIn_2S_4$ display upshift with respect to that of the pure $ZnIn_2S_4$ ultrathin nanosheets, as demonstrated by the UV/Vis absorption spectra and XPS valence band spectra. This elevated CB minimum and increased VB width can bring about a much higher mobility and better consumption of photogenerated holes, so as to favors the hydrogen production. Wang et al. found that doping C atoms can effective tune the electronic structure of h-BN (**Figure 7**).[93] On the basis of the DFT calculation, the band gap of

h-BN is determined to be 4.56 eV. After the C doped into the crystal lattice, the band gap can be significantly reduced. With respect to '$B_{11}C_{12}N_9$'-compound, the gap can be narrowed to 2.00 eV, with the VB and CB edges mainly composed of the C 2p orbitals. The VB top states of $B_{11}C_{12}N_9$ are more delocalized when compared with that of pristine BN. Benefiting from the carbon doping with sp^2 delocalized system, the obtained C-BN ultrathin nanosheets with the thickness about 3-4 nm can display excellent visible light photocatalytic behavior towards hydrogen evolution and CO_2 reduction. In view of the insulator feature of pure h-BN, it illustrate the non-metal doping can not only promote the photocatalytic performance but also in fact create emerging photocatalytic behavior.

3.4. Defect Engineering

Apart from doping, the defect engineering can also show significant influence on the ultrathin 2D materials towards photocatalysis. Since the 2D atomically-thin structure, the existence of defects will have strongly impact on the intrinsic properties, even with an extremely low concentration. Compared with the large formation energy of the surface defects in bulk materials, the ultrathin 2D nanosheets with relatively small atomic escape energy can offer a valuable opportunity to achieve various defects. Therefore, it is desirable to build artificially surface defect engineering such as anion vacancy, cation vacancy, vacancy associates, pits, and distortions, so as to effectively optimize the electronic structure of ultrathin 2D photocatalysts.[94]

3.4.1 Anion Vacancy

As a kind of anion vacancy, the oxygen vacancy has been widely studied since its low formation energy and ubiquity in oxide materials.[95] For instance, through the rapidly heating of the intermediate ultrathin $In(OH)_3$ nanosheets in air or in oxygen, the O-vacancies-rich and O-vacancies-poor ultrathin In_2O_3 nanosheets can be controlled prepared, respectively.[34] As shown in **Figure 8**, the AFM image exhibit the thickness of In_2O_3 nanosheets to be about 0.9 nm, revealing the controlled preparation of In_2O_3 materials with atomically-thin. The XPS spectroscopy and electron spin resonance (ESR) spectra are employed to determine the presence of oxygen vacancies. The O-

vacancy characteristic peak located at 531.4 eV can be found with the O-vacancies-rich ultrathin In_2O_3 nanosheets possess the highest peak area, suggesting more O-vacancies have been introduced relative to O-vacancies-poor ultrathin In_2O_3 nanosheets and bulk counterpart. In addition, the sharp O-vacancy signal at g = 2.004 in ESR spectra can also be observed, which indicates the O-vacancies-rich ultrathin In_2O_3 nanosheets sample hold the highest O-vacancy concentration. With the O-vacancy engineering, the electronic structure of O-vacancies-rich ultrathin In_2O_3 nanosheets will suffer from obvious variation. As certified by DRS analysis and XPS valence band spectra, the O-vacancies-rich ultrathin In_2O_3 nanosheets display a narrowed band gap and upshifted VB edge. According to DFT calculations, the obviously increased DOS at valence band maximum (VBM) can be formed and a new defect level appears in O-vacancies-rich ultrathin In_2O_3 compared with O-vacancies-poor ultrathin In_2O_3 nanosheets. As a result, the O-vacancies-rich ultrathin In_2O_3 nanosheets can acquire a higher carrier concentration and increased electric field in the space charge regions. The electrons can be more easily excited into the CB under irradiation. Benefiting from these features, the O-vacancies-rich ultrathin In_2O_3 nanosheets displayed 2.5 and 15 times increased photocatalytic behavior than O-vacancies-poor ultrathin In_2O_3 nanosheets and bulk In_2O_3, respectively towards water oxidation. This result undoubtedly demonstrated the effective role of anion vacancy for electronic structure tuning.

3.4.2. Cation Vacancy

Apart from anion vacancy, the cation vacancy is a very effectively pathway to result in attractive electronic structure variation of the ultrathin nanostructure thanks to the multifarious electron configuration and orbit. For instance, vanadium-vacancies have been controlled introduced to the single-unit-cell $BiVO_4$ nanosheets (1.28 nm thickness) with different concentrations (**Figure 9**).[60] The vanadium vacancy is affirmed on the atomic level by positron annihilation spectrometry and X-ray fluorescence (XRF). The shortest life component (τ1, around 200 ps) for the $BiVO_4$ samples is ascribed to the positron annihilation trapped at vanadium vacancy, revealing the existence

of vanadium vacancy in the two samples. The relative stronger intensity of positron lifetime in vanadium vacancy-rich $BiVO_4$ nanosheets meaning the higher vanadium vacancy concentration. Moreover, the element ratio of V and Bi is determined to be 0.914 and 0.976 for vanadium vacancy-rich $BiVO_4$ nanosheets and vanadium vacancy-poor $BiVO_4$ nanosheets, respectively, further suggesting the concentration difference of vanadium vacancy. Profiting from the presence of vanadium vacancy, a new defect level can be formed in the band gap of $BiVO_4$, as demonstrated by the DFT calculation, leading the electrons more able to be excited into the CB. In addition, the higher DOS at the VB edge can be obtained owning to the vanadium vacancy engineering. Therefore, the engineered vacancies can increase the light harvesting and promote the electronic conductivity in vanadium vacancy-rich $BiVO_4$. At the same time, the abundant vanadium vacancies enabled effective charge separation, which could prolong carriers' lifetime from 74.5 to 143.6 ns. Benefiting from these advantages derived from vanadium vacancies, a promoted photocatalytic performance can be achieved with methanol formation rate up to 398.3 μmol g^{-1} h^{-1}.

3.4.3. Vacancy Associates

With the missing of surface atoms, not only the mono-vacancies can be formed but also the vacancy associates are able to appear. Owing to the multi-atomic vacancy coupling, the vacancy associates may powerful tune the electronic structure and bring about extraordinary electronic behavior. For example, the triple vacancy associates $V_{Bi}'''V_O^{\cdot\cdot}V_{Bi}'''$ can be built in the BiOCl ultrathin nanosheets (2.7 nm thickness) with the dimension tuning (**Figure 10**).[63] The generated triple vacancy associates $V_{Bi}'''V_O^{\cdot\cdot}V_{Bi}'''$ is determined by the positron annihilation spectrometry. Due to the Bi atoms are exposed outside in BiOCl crystal structure, it is more prone to escape from the lattice to form the vacancy. When the thickness is reduced to atomically-thin, the oxygen atoms which connect to Bi atoms in internal layer can also escape more easily. Thereby, the dominating defects of BiOCl nanoplates is isolated V_{Bi}''' while change to vacancy associates $V_{Bi}'''V_O^{\cdot\cdot}V_{Bi}'''$ in BiOCl ultrathin nanosheets. The distinct defect types undoubtedly affect the electronic structure, which ensure the

BiOCl ultrathin nanosheets with improved adsorption of RhB molecules owning to the more negatively charged nature. Profiting from the defect types variation from V_{Bi}''' to $V_{Bi}'''V_O^{\cdot\cdot}V_{Bi}'''$, the BiOCl ultrathin nanosheets display both upshifted CB and VB potentials, which favors the charge mobility and thus enable the better separation of electron-hole pairs. As a consequence, the BiOCl ultrathin nanosheets show outstanding solar photocatalytic activity towards pollutants removal.

3.4.4. Distortions

In addition to vacancies, other defects such as distortions and pits are also feasible strategies to affect the electronic structure of ultrathin 2D photocatalysts.[27, 51] For example, O'Hare et al. prepared the NiTi-layered double hydroxides (LDH) nanosheets with the controlled thickness via a reverse microemulsion strategy.[45] The local atomic arrangement of the obtained NiTi-LDH nanosheets is analyzed by the X-ray absorption near-edge spectroscopy (XANES). When the thickness greatly reduced, a great deal of titanium cations in a lower oxidation state can be obtained in NiTi-LDH nanosheets (~2 nm thickness), while it is almost exclusively Ti^{4+} in bulk NiTi-LDH. Compared to bulk NiTi-LDH, the lower coordination numbers of Ti cations can be seen in NiTi-LDH nanosheets and suffer from serious structure distortions. As a result, the NiTi-LDH nanosheets show distinctive electronic structure and improved electron transfer efficiency relative to bulk NiTi-LDH.

3.4.5. Pits

The construction of pits affords a favorable method to increase the surface defects, which can create more coordination-unsaturated atoms with dangling bonds around the pits in nanosheets. By thermally treating bulk g-C_3N_4 under the NH_3 atmosphere, it can be effectively exfoliated to nanosheets and numerous in-plane pits can be constructed in the g-C_3N_4 nanosheets.[96] The constructed in-plane pits will destroy the plane structure of g-C_3N_4 layers and supply rich emerging active sites with dangling bonds and will also serve as cross-plane diffusion channels to accelerate the mass transfer and charge diffusion. What's more, the constructed pits will further result in the

formation of C vacancies due to the unbalanced structure destruction. As a consequence, the g-C_3N_4 nanosheets shows enlarged bandgap and extended light absorption region compared with bulk counterpart. At the same time, the pits-rich g-C_3N_4 nanosheets ensure an elevated CB and VB potential and provide higher electron donor density. Thereby, a 20 times higher photocatalytic hydrogen evolution activity can be achieved under visible light irradiation.

The above analysis results supply new and in-depth insights for understanding the mechanism of action of surface defects in promoting the photocatalytic performance from the energy band structure, surface charge, and active site aspects. Generally, compared with the defect-poor counterparts, the engineered defects in the ultrathin 2D materials can tune the electronic structure, usually with the increased DOS at the edge of the VB or CB, or even build new defect level among the forbidden band. Usually, the light absorption scope of the original materials can be red extended and light harvesting ability can be increased. The local charge density at the surface can also be tuned and may facilitate the adsorption and activation of target molecules. At the same time, the engineered surface defects can improve the carrier concentration in photocatalysts and serve as charge separation centers to trap carriers, promoting utilization efficiency of holes and electrons for corresponding interfacial redox reactions.

4. Hybridization

Different from that in bulk materials, the ultrathin 2D materials with atomically thickness possess ultra-large specific surface area, ensuring the surface state to be even more important than that in the bulk inside. The photogenerated charge carriers will diffuse to the surface to involve in the following redox reactions. Thereby, the surface hybridization to introduce foreign component to promote the utilization efficiency of charge carriers is desirable under the precondition of ultrathin 2D configuration. According to the surface hybridized types, several typical hybridizations with ultrathin 2D structures are presented, including quantum dot/2D materials, single atom/2D materials, molecular/2D materials, and 2D-2D stacking materials.

4.1. Quantum Dots/2D Materials

The coordination-unsaturated surface atoms of nanoparticles (NPs) have dangling bonds which cost energy. To further reduce the size of NPs, the larger fraction of surface atoms relative to total atoms can be achieved and their average binding energy per atom will be higher. Therefore, if size of NPs are controlled to quantum dots (QDs) and modified on the ultrathin 2D materials, the interfacial strong-coupling between QDs and ultrathin 2D materials can be build. Moreover, the QDs can display highly dispersion on the ultrathin 2D materials due to the small-size, which may be effective co-catalysts to further boost the photocatalytic activity. To improve the utilization efficiency of Ag, the Ag QDs with the size less than 5 nm is prepared.[97] After the hybridization with BiOBr nanosheets, the photocatalytic activity can be greatly improved towards the degradation of ciprofloxacin, tetracycline hydrochloride and rhodamine B under visible light irradiation. Studies found that the modified Ag QDs can active the molecular oxygen via the hot electron reduction under the visible light. The Ag QDs can simultaneous serve as adsorption centers, charge separation centers and photocatalytic reaction centers, which responsible for the improved photocatalytic performance.

To reduce the employment of noble metal, the non-noble metal or even metal-free QDs can be considered as alternative. Moreover, the thickness of the subject 2D materials can be further reduced to single layer, so as for better dispersion and interfacial contact. For instance, nitrogen-doped carbon quantum dots (N-CQDs) with the size of 3 nm have been controlled prepared via a facile hydrothermal process and then modified on the surface of atomically-thin BiOI nanosheets.[66] AFM images show the average thickness of BiOI is about 0.9 nm, suggesting the single-layer configuration. After the introduction of N-CQDs, the N-CQDs/BiOI materials display greatly prolonged lifetime of photogenerated charge carriers, as proved by time-resolved transient photoluminescence decay and instantaneous photocurrent. The atomically-thin structure of BiOI ensures the strikingly fast bulk charge diffusion to the surface and the modified N-CQDs with conjugated π structure can effective

promote the surface charge separation, result in a longer carrier lifetime. As a consequence, the photocatalytic activity and active species concentration of N-CQDs/BiOI materials improved significantly.

In another case, Kang et al. demonstrated that the CQDs can serve as chemical catalyst to extreme boost the photocatalytic water splitting by C_3N_4 (**Figure 11**).[98] Different from the conventional one-step four-electron reaction towards water splitting, the two-electron/two-electron two-step pathway can be achieved by CQDs-C_3N_4, in which the C_3N_4 contribute to convert the H_2O to H_2O_2 and H_2, and the CQDs is responsible for the H_2O_2 decomposition and O_2 generation. As a consequence, the excellent photocatalytic water splitting efficiency can be acquired, with 2.0% solar-to-hydrogen efficiency and robust stability in 200 runs of recycling use over 200 days. Apart from the above results, there also have several other systems regarding QDs/2D materials hybridization to further promote the photocatalytic performance, such as CdSe QDs, Zn-Ag-In-S QDs, NiS_2 QDs and so on.[99-102] These above results undoubtedly demonstrated the superiority of QDs modification and the QDs/2D configuration may be effective alternative structure to achieve high efficiency photocatalytic behavior.

4.2. Single Atom/2D Materials

To further boost the photocatalytic activity, reducing the size of modified nanoparticle to single atoms may be a feasible strategy, owing to the percentage of unsaturated coordination bonds of a single atom will maximization and enable a stronger surface effect.[103] Since the first proposed single-atom catalysis by Zhang et al., it has become a very hot project in catalysis field.[104] The single-atom catalyst is consist of isolated individual atoms on the surface of support with the form of dispersion or coordination. The single atoms can not only maximize the catalytic activity but also supply an alternative approach to adjust the selectivity. Since the highly active of single atoms, the chemical bonding between metal single atoms and 2D supports will become stronger and charge

transfer process will be easier. Thereby, it is highly desirable to construct single atom/2D materials to acquire a high photocatalytic activity.[105]

Wu et al. reported the isolated single Pt atoms as co-catalysts to promote the photocatalytic H_2 evolution activity of C_3N_4 nanosheets.[106] A simple liquid-phase reaction with C_3N_4 and H_2PtCl_6 coupled low temperature annealing is employed to prepare the Pt single atoms/C_3N_4. The high-angle annular dark-field scanning transmission electron microscopy (HAADF-STEM) is employed to determine the distribution and configuration of Pt (**Figure 12**). The distinct bright spots corresponding to Pt atoms can be observed to evenly dispersed on g-C_3N_4, with the size of 99.4% Pt species is less than 0.2 nm, revealing the Pt exists exclusively as isolated single atoms. It is worth noting that when the loading amount of Pt reach 0.38%, the dispersion of Pt atoms will be dense and will form several sub-nanometer clusters. The extended X-ray absorption fine structure (EXAFS) spectroscopy is used to probe the local atomic arrangement of Pt/C_3N_4. The coordination number of the Pt atoms is measured to be 5 with the bond distance of 2.03 Å, revealing the Pt atoms are dispersed on the top of the five-membered rings of the C_3N_4 network. After the construction of Pt single atoms/C_3N_4 structure, the photocatalytic hydrogen evolution activity can be greatly promoted. The hydrogen evolution rate of Pt-C_3N_4 (0.16 wt% Pt loading) can up to 318 μmol h^{-1}, approximately 50 times higher than the pure C_3N_4. At the same time, the Pt single atoms/C_3N_4 materials exhibit excellent stability for hydrogen evolution and the isolated Pt single atoms still keeps on the C_3N_4 after circulations. By virtue of the ultrafast transient absorption (TA) spectroscopy, the surface trap states of C_3N_4 has been demonstrated to be intrinsic changed due to the isolated Pt single atoms, which prolong the carrier lifetime and supply more opportunities for electrons to involve in the H^+ reduction process.

In addition, isolated Rh single atoms have been introduced to the 2D TiO_2 nanosheets with uniform thickness of 0.7 nm through calcination, protonation coupled exfoliation process.[107] From the HAADF-STEM image, the isolated brightest spots can be seen which represent Rh atoms, and

the spots with intermediate brightness means Ti atoms. According to the EXAFS, the Rh species in Rh single atoms/TiO_2 samples display a similar chemical environment as in Rh_2O_3, meaning the bonding to O atoms and thus are oxidized. The single Rh atoms co-catalyst can serve as reaction centers towards photocatalytic hydrogen evolution according to DFT calculation. As a result, the photocatalytic hydrogen evolution rate is 10 times increased in comparison to the pure TiO_2 nanosheets.

Although the single atom have been employed in catalysis, there also exist several issues to be resolved. Generally, the supported content of single-atom is relatively low and the noble metal single-atom dominate the major types. It is highly desirable to increase the amount of supported metal atoms with the isolated single atom structure and extend to more non-noble metals. Additionally, the stability need to be further promoted to meet the potential applications. The fact that isolated single metal atoms have high surface energy per atom reveal that the individual metal atoms can interact strongly with support surfaces. By manipulating the interactions of metal atoms with surface defects (high energy sites) on a support, the energy of the hybridization system may become a local minimum. As a result, the single metal atoms can be anchored and keep stability. Especially for the ultrathin 2D materials, the surface defects are prone to be formed due to the ultralarge specific surface area and small atomic escape energy. Therefore, it is feasible to build single atoms anchored surface defect-rich ultrathin 2D configuration to achieve high photocatalytic performance.

4.3. Molecular/2D Materials

Apart from isolated single atoms, the single molecular can also be employed to tune the electronic structure or serve as co-catalyst to effective boost the photocatalytic activity.[108, 109] Benefiting from the subnanopores in the C_3N_4, molecular titanium-oxide can be incorporated into C_3N_4 nanosheets through a facile polycondensation of precursors with dicyandiamide and titanium oxide ions (**Figure 13**).[110] The clean ultrathin sheet-like morphology can be observed from TEM

image and the thickness of the TiO-C_3N_4 nanosheet is determined to be 3-3.3 nm. According to the HAADF-STEM image and elemental mapping images, the titanium-oxide can be found to be homogeneously dispersed in the framework of C_3N_4 with the isolated format. This result suggest the molecular titanium-oxide has been successfully incorporated into the C_3N_4 framework homogeneously. The local electronic and geometrical structures of Ti-O in the subnanopores of C_3N_4 nanosheet is determined via XAFS. Generally, the anatase TiO_2 will display a well-defined triple pre-edge feature, which can be attributed to the distorted TiO_6 configuration with six coordinated oxygen atoms. Different from the result of TiO_2, the Ti-O structure in C_3N_4 exhibit the single pre-edge feature with non-central symmetry. As proved by the EXAFS, the Ti atom is indeed located in the hole of the C_3N_4, in which coordinated with six nitrogen atoms in C_3N_4 and one oxygen atom out of the C_3N_4 plane. Profiting from the molecular titanium-oxide incorporation, the TiO-C_3N_4 nanosheets display narrowed bandgap compared with pure C_3N_4 with the decrease of CB position. This is derived from the more electron contribution of Ti-O into the C_3N_4 and increase the π-electron delocalization in the conjugated system. The tuned electronic structure of TiO-C_3N_4 will further promote the separation of charge carriers. As a result, the TiO-C_3N_4 can display improved photocatalytic activity for the generation of •OH and pollutant removal.

During the photocatalytic process, the sluggish kinetics of hole transfer and then bring about massive carrier recombination have been the Achilles' heel of photocatalytic conversion performance. Although the ultrathin 2D structure allow the rapidly charge migration during the bulk phase, the absence of surface charge separation centers will also damage the overall photocatalytic efficiency. Employing strategies to promote the surface charge separation, especially the hole transfer is highly desirable. As an alternative, it seems feasible to use water-soluble molecular as homogeneous co-catalyst, so as to further optimize the photocatalytic behavior. For example, Wu et al. developed water-soluble molecular trifluoroacetic acid (TFA) as co-catalysts to boost the photocatalytic hydrogen evolution activity of $K_4Nb_6O_{17}$ nanosheet.[111] Profiting from the reversible redox couple

TFA•/TFA$^-$ and highly active intermolecular radical reactions, the TFA molecule can serve as a robust hole shuttle, allowing effective transfer of photogenerated holes and resulting high charge separation efficiency. With the increase of TFA, the hydrogen evolution rate improved gradually and the optimized rate can reach 6,344 μmol g^{-1} h^{-1} when the molar ratio of TFA/$K_4Nb_6O_{17}$ is 25.6. This optimal hydrogen evolution rate is roughly 32 times higher relative to the pure $K_4Nb_6O_{17}$ nanosheets, undoubtedly demonstrating the advantage of this molecular co-catalyst.

Owing to the solid-state co-catalysts is limited by finite contact areas between co-catalysts and host photocatalyst, the surface charge separation cannot be fully guaranteed. If overmuch solid-state co-catalysts is anchored on the photocatalyst, the active sites will be covered and lacking of sufficient active sites accessible to the reactant molecules. By virtue of water-soluble, these molecular co-catalysts can homogeneous dispersed in solution and can provide maximum accessible area to the host photocatalysts. Thereby, the developed molecular co-catalyst strategy may be a feasible pathway for efficient separation of photogenerated carriers, and hence promote the photocatalytic behavior.

4.4. 2D-2D Stacking Materials

Building 2D-2D stacking is another widely used strategy to optimize the photocatalytic performance. Especially for the layered materials, the lattice mismatch can be minimized owing to the similar layered structures, and 2D-2D stacking with intimate contacts can be constructed. For instance, Zhang et al. prepared the single-layered $Bi_{12}O_{17}Cl_2$ with surface oxygen vacancies through the lithium intercalation-based exfoliation strategy.[81] Subsequently, MoS_2 monolayers are assembled onto the single-layered $Bi_{12}O_{17}Cl_2$ via the surface oxygen-vacancies and build the Bi-S bonds between $Bi_{12}O_{17}Cl_2$ and MoS_2. As shown in **Figure 14**, the TEM image coupled with elemental mapping images suggest that many small MoS_2 nanosheets are tightly anchored on a large $Bi_{12}O_{17}Cl_2$ nanosheet to form 2D-2D stacking heterostructure. From the AFM images, it demonstrate the average thickness of the large-sized and small-sized nanosheets are 0.717 and 0.686, which

accord with the $Bi_{12}O_{17}Cl_2$ and MoS_2 single layers, respectively. View from the atomic-resolution HAADF-STEM image and the corresponding EELS elemental maps, it can be clearly observed that the MoS_2 single layers are anchored selectively on the $(Bi_{12}O_{17})$ end-faces to build (Cl_2)-$(Bi_{12}O_{17})$-(MoS_2). Due to the charge density surrounding $(Bi_{12}O_{17})^{2+}$ layer is higher than that of $(Cl_2)^{2-}$ layer, the photogenerated electrons and holes will be driven to $(Bi_{12}O_{17})^{2+}$ and $(Cl_2)^{2-}$ end-faces under the irradiation, respectively. Then, the photogenerated electrons will flow to the MoS_2 single layers via the formed Bi-S bonds, enabling the effective charge separation (ultralong carrier lifetime of 3446 ns), as evidenced by the transient absorption (TA) spectroscopy. Benefiting from the atomically-thin thickness, effective orientated interface charge separation and abundant hydrogen-evolving sites in MoS_2, the obtained $MoS_2/Bi_{12}O_{17}Cl_2$ bilayers display outstanding visible light photocatalytic hydrogen evolution behavior. With the ascorbic acid as hole sacrificial agent, the hydrogen evolution rate can arrive at 33 mmol h^{-1} g^{-1} and the quantum efficiency of 36% at 420 nm.

Apart from the $MoS_2/Bi_{12}O_{17}Cl_2$, there have numerous reports regarding 2D-2D stacking to optimize the photocatalytic performance, such as $NiO/Ca_2Nb_3O_{10}$,[112] MoS_2/TiO_2,[113] MoS_2/CdS,[114] WS_2/CdS,[114] MoS_2/C_3N_4,[115] SnS_2/C_3N_4,[116] Fe_2O_3/C_3N_4,[117] $C_3N_4/Bi_4O_5I_2$,[118] ZnCr-LDH/layered titanate,[119] $ZnIn_2S_4/MoSe_2$,[120] and so on. Such a unique 2D-2D stacking structure has some advantages. It can increase the accessible area around the planar interface of the 2D and 2D layers, and reduce the barriers for electron transport through the co-catalyst, thus promoting the interfacial charge transfer process by the electron tunneling effect. Moreover, this 2D thin layers can relieve the light blocking effect of the co-catalyst, thus adequate light can access to the host photocatalyst. It is desirable to tune the 2D component and strengthen the interfacial acting force to further build high-efficiency 2D/2D photocatalysts.

5. Photocatalytic applications

According to the above mentioned results, the ultrathin 2D materials can display enormous advantages towards the photocatalysis from the microstructure, electronic structure, energy band

structure and surface property. Up to now, the advanced ultrathin 2D materials have been applied as photocatalysts for diverse photocatalytic applications. Herein, the advancement of versatile photocatalytic applications by ultrathin 2D materials in the fields of water oxidation, hydrogen evolution, CO_2 reduction, nitrogen fixation, organic syntheses, and pollutants removal will be discussed **(Table 1)**.

5.1. Water Oxidation

It is widely recognized that the hydrogen is one of the most promising green fuels with the advantages as high specific energy, multiple utilization modes and clean combustion product. It will display grand prospect for future sustainable energy consumption if it is generated via a sustainable technology. Photocatalytic water splitting into hydrogen and oxygen is regarded as the Holy Grail during the chemistry field with only the sustainable solar light as energy input, photocatalysts as medium and water as reaction source. Although significant breakthroughs have been achieved, the efficiency of water splitting is still limited for most photocatalytic systems. Generally, the water oxidation is the efficiency-limiting process in the photocatalytic water splitting systems due to the complex four-hole involved redox process. Thereby, it is high desirable and urgent to design the photocatalyst with robust solar water oxidation performance. Recently studies found that the ultrathin 2D photocatalysts are promising alternative towards solar water oxidation.[16, 27, 30, 34, 45, 50-52, 55] The freestanding ZnSe single layers with four-atomic thickness have been controlled prepared via a lamellar hybrid intermediate (Zn_2Se_2)(pa) (pa represent n-propylamine) strategy with ultrasonic exfoliation.[55] Through the X-ray absorption fine structure (XAFS) measurement, the local atomic arrangements and electronic structures of the obtained ZnSe single layers can be determined. As shown in the Zn *K*-edge $k\chi(k)$ oscillation curves (**Figure 15a**), the ZnSe single layers display obvious distinction relative to ZnSe-pa single layers and bulk ZnSe, indicating the remarkable difference of local atomic arrangement. To make a more explicitly expression, the R-space curves of ZnSe samples are shown in **Figure 15b**. The peaks located at 2.11 and 3.63 Å are ascribed to the nearest

Zn-Se and next nearest Zn-Zn coordinations in the bulk ZnSe. When the thickness of ZnSe is reduced to atomically, the local atomic arrangement undergo remarkable variation. The Zn-Se peak is shift to 2.17 Å and the next nearest Zn-Zn distances (3.85 Å) are contracted. At the same time, the Se-Se distances in ZnSe single layers are elongated from 4.012 Å of bulk ZnSe to 4.11 Å. These results undoubtedly demonstrate the existence of surface distortion within the single layer structure, which will reduce the surface energy and enable the outstanding stability of ZnSe single layers. In addition, the surface distortion of single-layered ZnSe will result in the increased density of states at the CB edge, which can further ensures a high migration rate of charge carriers (**Figure 15c**). Benefiting from the single-layered structure with surface distortion, the ZnSe single layers display stronger light absorption, increased charge separation efficiency and smaller charge transfer resistance. As a consequence, the ZnSe single layers exhibit 195 times higher photocatalytic activity than bulk ZnSe towards water oxidation under Xe lamp irradiation (**Figure 15d**).

Owing to the water oxidation to produce oxygen is an absolute hole participated reaction, improving the hole utilization rate may be an effective strategy to further boost the photocatalytic water oxidation efficiency. Liu et al. construct numerous pore structure in the WO_3 ultrathin nanosheets via the fast-heating strategy on the beforehand exfoliated $WO_3 \cdot 2H_2O$ nanosheets.[27] Since the migration direction of the photogenerated holes is along the W-O-W chains in the x direction in the {001} facets exposed WO_3 nanosheet, the longish migratory route of photogenerated holes will inevitably undergo numerous recombination of charge carriers, which will seriously hindering the photocatalytic behavior. The constructed pores will effective shorten the diffusion pathway of holes and conduce to water oxidation to form O_2 on the WO_3 surface. In addition, the abundant dangling bond along pore surroundings can create a favorable condition to facilitate chemisorptions of reaction molecular, eventually boosting the oxygen evolution kinetics. As a consequence, 18 times higher photocatalytic water oxidation performance can be obtained for pore-rich WO_3 ultrathin nanosheets relative to bulk WO_3. It reveals important guidelines for promoting the

conversion efficiency by using ultrathin 2D structure towards photocatalytic water oxidation. In addition, numerous other photocatalysts with ultrathin 2D structure can also display outstanding photocatalytic behavior towards water oxidation, such as SnS_2,[51] SnS, SnSe,[50] Fe_2O_3,[30] NiTi LDH,[45] and further tuned materials like oxygen vacancies engineered In_2O_3,[34] Co doped In_2S_3,[52] pit-rich BiOCl,[121] and so on.

5.2. Hydrogen Evolution

Since the groundbreaking research for the photocatalytic hydrogen evolution over TiO_2 in 1972, the photocatalytic hydrogen evolution from water is at the forefront of chemistry research towards solving the global energy crisis. Although a lot of impressive materials have been developed towards photocatalytic hydrogen production, most of them are still subjected to fairly low photocatalytic efficiency, far from sufficient to meet the requirements of practical applications. Recent studies regarding 2D materials found that the emerging ultrathin 2D semiconductors with the suitable energy band structure are promising alternative to reach the excellent hydrogen evolution efficiency.[122] Among the abundant semiconductors, Cu_2O with the special CB position lying 0.7 V negative than the hydrogen evolution potential, may be an efficient catalyst for solar-to-hydrogen conversion. To realizing the high hydrogen evolution behavior, the 2D atomically-thin sheet-like structured cubic Cu_2O is controlled prepared.[31] Through the AFM image, the thickness of the Cu_2O nanosheets is determined to be 0.62 nm, corresponding to 4 atomically-thick Cu_2O slab along the [01-1] direction. As is well known, the surface energy of cubic Cu_2O comply with the order of (111) < (100) < (110). Since the (110) and (01-1) facets are the equal facets, the (01-1) facet in atomically-thin Cu_2O nanosheets can also exhibit large surface energy, which will bring about an efficient activity. With the significantly decrease of thickness, the electronic structure of the atomically-thin Cu_2O nanosheets will be distinct from the bulk counterpart. Through the DFT calculations, atomically-thin Cu_2O nanosheets display greatly improved density of states at the edge of VB with respect to bulk Cu_2O. At the same time, the extended CB edge can also be observed for atomically-thin Cu_2O

nanosheets relative to bulk Cu_2O, revealing the atomically-thin Cu_2O possess higher carrier mobility and narrower band gap. Benefiting from these advantages, more than 36 times higher photocatalytic hydrogen evolution rate can be acquired by atomically-thin Cu_2O nanosheets under visible light irradiation. This result undoubtedly demonstrates that the ultrathin 2D structure can bringing enormous superiority for hydrogen evolution and also a series of unprecedented performances.

To further promote the hydrogen evolution efficiency, further tuning based on the 2D ultrathin structure can be employed. For example, by doping oxygen into the $ZnIn_2S_4$ nanosheets, the hydrogen-evolution rate of the O-doped $ZnIn_2S_4$ can reach 2120 μmol $h^{-1}g^{-1}$ from aqueous solution containing 0.25 M Na_2SO_3 and 0.35 M Na_2S under the visible light irradiation without any co-catalyst, which is 4.5 times higher than pristine $ZnIn_2S_4$ (**Figure 16**).[53] The local atomic structures of the prepared samples are characterized through the XAFS. The oxygen doping in the $ZnIn_2S_4$ nanosheets can create high structural distortion by the substitution of oxygen atoms for sulfur. Owing to the tuned local atomic structures, the electronic structure will suffer from obvious variation. Through the DFT calculation, it can be found that the oxygen doping can increase the DOS at VB maximum relative to pristine $ZnIn_2S_4$, suggesting the formation of increased charge density around the VBM. According to the XPS valence spectra and the estimated band gap, it can be seen that both the CB minimum and VB maximum of O-doped $ZnIn_2S_4$ ultrathin nanosheets show upshifting when compared with the pristine $ZnIn_2S_4$. As a result, the average recovery lifetime of carriers for O-doped $ZnIn_2S_4$ nanosheets is roughly 1.53 times longer when compared with pristine $ZnIn_2S_4$, reaching 110 ps. Profiting from these advantages, the O-doped $ZnIn_2S_4$ can exhibit greatly improved photocatalytic behavior for hydrogen evolution. These above results suggest the doping is an effective strategy to tune the local atomic structures and electronic structure of 2D materials, further affect the charge migration or separation, and finally optimize the hydrogen evolution performance.

In addition, considering the major ultrathin 2D semiconductors are lack of sufficient hydrogen-evolving sites, it is desirable to introduce abundant hydrogen-evolving sites such as single atom Pt or

few-layered transition metal dichalcogenides to further boost the hydrogen evolution behavior. For example, Wang et al. introduced few layer MoS_2 to C_3N_4 to optimize the photocatalytic hydrogen evolution efficiency.[115] During the preparation process, the C_3N_4 is immersed into an aqueous solution of $(NH_4)_2MoS_4$, and then sulfidation with H_2S gas at 350 ºC. The fact that C_3N_4 and MoS_2 have analogous layered structures can minimize the lattice mismatch and favors the planar growth of MoS_2 slabs over the C_3N_4 surface, so that building an organic-inorganic 2D-2D stacking with graphene-like thin layered heterojunctions. Abundant hydrogen evolving sites can be provided by few layer MoS_2. In addition, the thin layers of MoS_2 dispersed on the C_3N_4 surface can supply much higher efficiency than multi-layered MoS_2 due to the electron-tunneling effect through the MoS_2 thin layers to reaction interfaces. By virtue of the promoted charge separation efficiency and abundant hydrogen evolving sites induced by few layer MoS_2, the obtained MoS_2/C_3N_4 2D junctions exhibit superior photocatalytic hydrogen evolution performance than pure C_3N_4. The optimal sample with 0.2 wt% MoS_2 can show the highest hydrogen evolution rate, with an apparent quantum yield of 2.1% measured at 420 nm. Despite these advances and effects, there still face challenges for photocatalytic hydrogen evolution. The sacrificial electron donor and noble-metal cocatalyst are generally required in most hydrogen evolution systems. The solar overall water splitting is rather a challenge to achieve a high efficiency. It is expected that more high-efficiency ultrathin 2D photocatalysts be developed and coupled with proper tailoring to give an astonishing photocatalytic hydrogen evolution behavior.

5.3. CO_2 Reduction

Apart from photocatalytic hydrogen evolution, CO_2 reduction to yield hydrocarbon fuels over photocatalysts has been regarded as an effective means to simultaneous relieve the energy crisis and the greenhouse effect. Generally, the CO_2 molecule is extremely stable with the dissociation energy of C=O bond higher than 750 kJ mol^{-1}. Therefore, during the CO_2 photoreduction process, the high energy input is needed to break the O=C=O double bonds, which is much more challenging than

splitting water into hydrogen. The first step for the formation of a $CO_2^{\cdot-}$ intermediate via single electron transfer to activate CO_2 has been regarded as the rate-limiting step towards the subsequent proton-involved reduction process. An equilibrium potential of -1.9 V versus NHE is required theoretically for the first activation step and herein a higher overpotential is essential for real applied potentials. Moreover, multiple proton-coupled electron transfer processes are involved in the activation of CO_2 and the reaction pathways are rather complex and diversity with the formation of various products. According to the different number of injected electrons ($2e^-$, $4e^-$, $6e^-$, and $8e^-$), the products such as CO, HCHO, CH_3OH, and CH_4 can be achieved, respectively. In addition, there exist competition between the CO_2 photoreduction and the reduction of H_2O since the H_2O reduction to yield H_2 is kinetically more favorable, which further limit the selectivity of products.

Recent studies found that ultrathin 2D photocatalysts can display excellent CO_2 photoreduction performance.[24, 43, 57, 60, 123] For example, the Bi_2WO_6 layers with single-unit-cell thickness is controlled prepared via a lamellar hybrid intermediate strategy.[57] The sodium oleate is employed to supply oleate ions so as to interact with Bi^{3+} through electrostatic interaction. Subsequently, the lamellar Bi-oleate complexes can be constructed via self-assembly with head-to-head (or tail-to-tail) bilayer arrangement of oleate ions to build a mesostructure. When the Na_2WO_4 is added and threated with hydrothermal process, the Bi_2WO_6 can be produced and the lamellar mesostructure is self-exfoliated into single-unit-cell layers. The prepared single-unit-cell Bi_2WO_6 layers is employed as photocatalyst for CO_2 photoreduction measurement and a 300 W Xe lamp with a standard AM 1.5G filter is serve as light source. During the measurement, Bi_2WO_6 powder is suspended in water with high purity CO_2 gas continuously bubbled throughout the solution. An average rate of 75 $\mu molg^{-1}$ h^{-1} can be achieved for the formation of methanol over single-unit-cell Bi_2WO_6 layers within 5 h test, which is about 3 and 125 times higher relative to the Bi_2WO_6 nanocrystals and bulk Bi_2WO_6, respectively. After sixth cycles, the photoreduction efficiency do not suffer from any deterioration, revealing the excellent photostability. Studies found that the outstanding photocatalytic behavior is

derived from the unique geometric structure of single-unit-cell Bi_2WO_6 layers. Firstly, the ultra-large surface area of single-unit-cell Bi_2WO_6 layers ensures a 3-times higher capacity for CO_2 adsorption, which is the critical point for the activation and reduction of CO_2. Secondly, the single-unit-cell thickness contribute to promote charge separation and prolong the carriers lifetime, as testified by time-resolved fluorescence emission spectra measurements. Thirdly, single-unit-cell thickness bring about higher DOS at the CB edge and increase surface charge density, and thereby promote the two-dimensional conductivity. This study undoubtedly demonstrate the advantages of ultrathin 2D photocatalyst towards CO_2 photoreduction.

The adsorption of CO_2 is the important prerequisite for CO_2 photoreduction, which significantly affect the electron transfer process. Herein, it is desirable to found appropriate strategy to increase the adsorption site for CO_2 adsorption and build strong interaction to facilitate electron transfer for effective activation. Studies found that building surface defect sites may be an alternative means.[43] Through the controlled synthesis, the ZnAl-LDH ultrathin nanosheets with the thickness of 2.7, 4.1 nm and bulk ZnAl-LDH with the thickness about 210 nm can be prepared, which named as ZnAl-1, ZnAl-2 and ZnAl-3, respectively (**Figure 17**). When the thickness of bulk ZnAl-LDH is decrease to ultrathin structure, the density of oxygen-vacancy (V_o) defects will increase, thus will decrease the coordination number of neighbor Zn ions and introduce numerous coordinatively unsaturated Zn ions. Therefore, the Zn^+-V_o complexes can be constructed in the ultrathin ZnAl-LDH nanosheets, as certified by XAFS, electron spin resonance (ESR) and positron annihilation spectra measurements. During the CO_2 photoreduction process, the formed Zn^+-V_o complexes can work as trapping sites to promote the CO_2 adsorption. At the same time, as proved by the EIS and DFT calculation, the Zn^+-V_o complexes can also serve as electron trapping sites to enhance the charge separation efficiency and facilitate electron transfer to CO_2. As a consequence, the defect-rich ultrathin ZnAl-LDH nanosheets displayed outstanding photocatalytic behavior for the conversion of CO_2 into CO via a two-electron process with a conversion efficiency of 7.6 $\mu mol\ g^{-1}\ h^{-1}$ for ZnAl-1 sample.

To further boost the CO_2 conversion efficiency, improve the stability and selectivity, Xie's group engineering vanadium vacancy (V_v) into single-unit-cell o-$BiVO_4$ and employed as photocatalyst for CO_2 reduction.[60] With the assistant of cetyltrimethylammonium bromide, a lamellar hybrid intermediate strategy is employed for the preparation of o-$BiVO_4$ layers with single-unit-cell thickness. Through the regulation of reaction temperature and time, V_v-rich and V_v-poor o-$BiVO_4$ atomic layers can be obtained with [001] orientation. TEM and AFM images demonstrate the atomically thick of the o-$BiVO_4$ samples. As proved by positron annihilation spectrometry and X-ray fluorescence, V_v with distinct concentrations have been engineering on the surface of V_v-poor o-$BiVO_4$ and V_v-rich o-$BiVO_4$ samples. The formed V_v play important role during the photocatalytic process towards CO_2 reduction. First of all, the engineered V_v can create a novel defect level in the band gap and increase the hole concentration near Fermi level. As a consequence, the light harvesting of V_v-rich o-$BiVO_4$ is enhanced and the electronic conductivity is promoted. For another, thanks to the higher V_v concentration, the V_v-rich o-$BiVO_4$ display higher CO_2 adsorption capacity and stronger surface hydrophilicity relative to the V_v-poor o-$BiVO_4$, which undoubtedly instructive to the CO_2 reduction process. Finally, the engineered V_v can promote the charge separation and effective increase carriers lifetime, which allow more electrons to involve in the CO_2 photoreduction. Benefiting from the above mentioned advantages, the V_v-rich o-$BiVO_4$ exhibits an increased conversion efficiency with the methanol formation rate reaching 398.3 μmol g^{-1} h^{-1}. During the photoreduction process, only a small amount of H_2 and trace amount of ethanol can be detected, suggesting the high product selectivity. Moreover, the V_v-rich o-$BiVO_4$ can suffer from continue photoreduction reaction up to 96 h, without any obvious loss of photocatalytic activity. These above studies demonstrate that the ultrathin 2D photocatalysts are effective alternative for realizing the high-efficiency CO_2 reduction.

5.4. Nitrogen Fixation

Compared with CO_2 reduction, photocatalytic nitrogen fixation is even more challenging since the dissociation enthalpy of N≡N triple bond of molecule nitrogen is as high as 962 kJ mol^{-1}. Generally, the catalytic conversion of N_2 is extreme tough owing to the N_2 binds only weakly interplay with solid-state catalysts and the reaction involves high-energy intermediates. Therefore, it is highly desirable to perform suitable design to promote the convert efficiency of N_2 to ammonia. For instance, the reduction potential to form N_2^- is as high as -4.2 V versus NHE through $N_2 + e^- \rightarrow N_2^-$ process, while the proton-coupled electron transfer reaction $N_2 + H^+ + e^- \rightarrow N_2H$ has a more accessible reduction potential E^0 of -3.2 V versus NHE.[124] The proton assisted conversion process may avoid the generation of high energy intermediates and thus decrease the thermodynamic barrier for ammonia production. Recent studies demonstrate that the 2D materials may be a promising candidate to achieve the efficient photocatalytic nitrogen fixation.[125] Zhang et al. found that engineering oxygen vacancies into BiOBr nanosheets can effective promote the nitrogen fixation reaction.[126] Through the theoretical calculation, it can be found that when the N_2 is adsorbed onto oxygen vacancies via an end-on configuration, the adsorbed N≡N triple bond can be prolonged from 1.078 Å in the original N_2 to 1.133 Å, suggesting the effective activation of N_2. The produced electrons in BiOBr can easily injected into the π antibonding orbitals of N_2. With the availability of localized electrons for π-back-donation, the electrons in the oxygen vacancies can effective transfer to the adsorbed N_2 to make an activation. As a consequence, the N_2 reduction to ammonia catalyzed by BiOBr with oxygen vacancies require a very low energy barrier and a high photocatalytic activity can be achieved. The N_2 conversion rate can reach 104.2 μmol g^{-1} h^{-1} under visible light and 223.3 μmol g^{-1} h^{-1} under UV-vis light irradiation without the utilization of hole scavenger or cocatalyst. Inspired by the oxygen vacancy induced N_2 activation, the ultrathin MoS_2 with S vacancy is controlled prepared and further be applied to nitrogen fixation.[49] Studies found that the ultrathin MoS_2 can display an ammonia synthesis rate of about 325 μmol g^{-1} within 10 h measurement under the irradiation of simulated solar light. However, the commercial bulk MoS_2 cannot show any

photocatalytic activity towards ammonia formation under the same test condition, revealing the unique advantage of ultrathin MoS_2 towards N_2 reduction. According to the Mott-Schottky spectra, the CB position of the ultrathin MoS_2 and bulk MoS_2 samples can be estimated to be -0.35 V, and -0.24 V, respectively, which is located below the thermodynamic reduction potentials N_2 reduction reaction by one-electron or two-electron transfer process. Thereby, it can be deduced that the N_2 reduction over ultrathin MoS_2 is a multi-electron coupled proton transfer process. Owing to the essence of n-type semiconductor, there exist numerous free electrons in ultrathin MoS_2, and these free electrons can couple with the photogenerated excitons to create charged excitons (trions) in which mainly located around the Mo sites. The formed trions possess multiple electrons in one bound state, which is instructive to multi-electron transfer reactions. When the N_2 is captured by the S vacancies, it will be surrounded by three Mo atoms with the trions under light irradiation. The N_2 will be activated upon donating electrons from its bonding orbitals and accepting electrons to its three antibonding orbitals, resulting in a trions assistant six-electron reduction process.

The critical point of the photocatalytic N_2 fixation lie in the construction of adsorption site for molecule nitrogen, electron-rich systems for electron donation, tuning the band structure with sufficient reduction potential and coupling protons to low the energy requirement of intermediates.

5.5. Organic Syntheses

With the purpose of reducing energy consumption towards chemical manufacturing, solar light driven chemical transformation with the assistance of semiconductors hold great prospect. Under the irradiation, the semiconductor materials can harvest solar light to create excitons or hot carriers which can awaken chemical reactions on the catalyst surface. However, the photocatalytic conversion efficiency and the selectivity are still unsatisfactory towards lots of transformation processes in general. The weak interplay of molecular oxygen with the surfaces of photocatalysts, especially with defect-free surfaces, is a crucial issue account for the poor efficiency of photocatalytic organic syntheses. The reaction involved molecular oxygen require effective

interfacial electron transfer, either directly as a reactant or indirectly as an electron acceptor.[127] Another important issue is the poor selectivity, which may resulted from the photogenerated holes. The generated holes are generally with strong oxidizing power and can be responsible for the non-selective over-oxidation. Recently, the ultrathin 2D photocatalysts display great potential for selective organic transformation under mild conditions. For example, Xiong et al. engineering oxygen vacancies into WO_3 nanosheets to activate oxygen molecules and trigger the organic transformation.[128] The defect-rich WO_3 nanosheets is synthesized by calcining the first prepared $WO_3 \cdot H_2O$ nanosheets at 673K in N_2 atmosphere, while the defect-deficient WO_3 nanosheets is obtained by calcination in air atmosphere. From the aberration-corrected HAADF-STEM, it can be seen that the defect-deficient WO_3 display a relatively flat and smooth surface. At the same time, the continuous and ordered lattice fringes can be observed from the atomic-resolution HAADF-STEM image (**Figure 18**). These result unquestionable suggest the deficiency of defects in this defect-deficient WO_3 sample. With respect to the defect-rich WO_3 sample, the numerous small pits can be observed from the STEM image, as well as slight lattice disorder and dislocation appears in the nanosheets, which forceful highlighting the existence of numerous defects. To further disclose the existence of oxygen vacancies, the synchrotron radiation-based XAFS spectroscopy is carried out. The defect-rich WO_3 display obvious different local atomic arrangements relative to defect-deficient WO_3, in which the coordination numbers of W atom decrease from 6 for defect-deficient WO_3 to 5.4 for defect-rich WO_3, revealing the local deficiency of oxygen atom. The electron spin resonance (ESR) analysis is further employed to measure the WO_3 samples. Obviously, a symmetrical ESR signal at $g = 2.002$ can be observed for defect-rich WO_3, indicating the electron trapping at oxygen vacancies. Combine with the STEM, XAFS and ESR result, it suggest the existence of oxygen vacancies at specific locations and induces some lattice disorder and dislocation. Benefiting from the defect-rich structure, the O_2 can be chemisorbed at the oxygen vacancy of defect-rich WO_3 nanosheets via an end-on configuration and accompanying with electron transfer from the

coordinatively unsaturated site to O_2. As a result, the O_2 can be effective activated to $O_2^{\bullet-}$ species over defect-rich WO_3 and it can transform amines to corresponding imines with a 6 times increased kinetic rate relative to defect-deficient WO_3. With the reaction time extended to 8 h, the conversion ratio of benzylamine can be higher than 80 % with an extreme high selectivity and no obvious deterioration can be seen within 6 times catalytic cycles.

Apart from the molecular oxygen activation, the hydrophobicity is another important factor to affect the photocatalytic organic conversion process. Li et al. employed a colloidal synthesis strategy for the preparation of BiOCl ultrathin nanosheets.[129] Through the hydrolysis of $BiCl_3$ in octadecylene solution, assisted by in situ formation of water via reaction between oleylamine and oleic acid, the single-crystalline BiOCl colloidal ultrathin nanosheets (BiOCl C-UTNSs) can be obtained with the thickness about 3.7 nm. For make a comparison, BiOCl nanosheets with ultrathin thickness is also prepared via the hydrothermal route, named as BiOCl H-UTNSs. The surface water contact angle (CA) measurement is employed to determine the wettability of the as-synthetized BiOCl samples. The BiOCl C-UTNSs display a water CA of 116.3°, suggesting the hydrophobic nature. This is come from that the organic ligands are cap on the surface of BiOCl C-UTNSs through the colloidal synthesis route. In contrast, the BiOCl H-UTNSs exhibit a water CA of 0°, superhydrophilic nature of the obtained BiOCl H-UTNSs. The huge difference between the BiOCl C-UTNSs and BiOCl H-UTNSs may bring about significant influence for the photocatalytic organic conversion process. Additionally, there exist abundant oxygen vacancies on BiOCl C-UTNSs, resulting in the strong light absorption among the visible light range. Benefitting from the hydrophobic nature and increased light harvesting ability, the BiOCl C-UTNSs display greatly improved photocatalytic activity for the conversion of N-t-butylbenzylamine to the N-t-butylbenzylimine. The 78% conversion ratio can be acquired by BiOCl C-UTNSs, while the BiOCl H-UTNSs can only display 15% conversion rate under Xe lamp irradiation for 1 h. Moreover, the BiOCl C-UTNSs sample can be further employed for converting the secondary amines to the

corresponding imines with a high conversion efficiency and selectivity. The ultrathin 2D photocatalysts have been demonstrated to be promising alternative for photocatalytic organic syntheses and these insights can widen our understanding of organic transformation processes, and are beneficial to establishing more efficient organic transformation systems.

5.6. Pollutants Removal

With the rapid development of economic and accelerated industrialization, the environmental pollution problem has become a major issue to threaten public health. Semiconductor photocatalysis has been regarded as an effective and economic technology to handle the removal of environmental pollutions. Profiting from the unique advantages such as superior adsorption ability of pollutants and strong light harvesting capacity, the ultrathin 2D photocatalysts show great prospect for the pollutant removal. For example, Xia et al. prepared the $Bi_4O_5Br_2$ ultrathin nanosheets via a reactive ionic liquids assisted solvothermal route combine with pH adjusting.[82] The long carbon chain in the ionic liquids can serve as capping reagent which restrain the crystal growth along the c axis direction. At the same time, the pH value of the reaction condition is adjusted to 11, which can supply OH^- to replace the Br^- to perform dehalogenation during the formation process of $Bi_4O_5Br_2$. As a result, both the thickness and component tuned $Bi_4O_5Br_2$ materials is controlled prepared. The obtained materials is employed for the photocatalytic degradation of antibiotic ciprofloxacin (CIP) and tetracycline (TC) under visible light irradiation. After the irradiation for 120 min, 75% of CIP can be photodegraded by $Bi_4O_5Br_2$ while the degradation rate of BiOBr is 51.4%. Moreover, the $Bi_4O_5Br_2$ ultrathin nanosheets can display a degradation rate of 77.8% towards TC within 60 min irradiation, much higher than that of BiOBr with only 31.7%. The variable energy band structure of $Bi_4O_5Br_2$ is demonstrated to account for the increased photocatalytic performance. The more negative CB position of $Bi_4O_5Br_2$ will facilitate the formation of more active $O_2^{\bullet-}$ species. The upshifting of the CB position and the wider valence band will beneficial to the improved charge separation efficiency. As a result, the obtained $Bi_4O_5Br_2$ ultrathin nanosheets display superior behavior towards pollutant

removal. To further promote the photocatalytic activity for pollutant degradation, constructing surface defects may be an alternative strategy. Xie et al. found that when the thickness of BiOCl is decrease from 30 nm to 2.7 nm, the defect type in BiOCl will vary from isolated defects V_{Bi}''' to triple vacancy associates $V_{Bi}'''V_O^{\cdot\cdot}V_{Bi}'''$, as proved by the positron annihilation spectra.[63] By virtue of the triple vacancy associates $V_{Bi}'''V_O^{\cdot\cdot}V_{Bi}'''$ with four negative charges, the ultrathin BiOCl nanosheets are more negatively charged relative to BiOCl nanoplates. Since the RhB is positively charged, the more negatively charged BiOCl ultrathin nanosheets can promote the adsorption of RhB on the surface of BiOCl ultrathin nanosheets. In addition, the existence of vacancy associates can increase the light absorption and accelerate the charge separation. As a consequence, the BiOCl ultrathin nanosheets can exhibit outstanding solar photocatalytic activity for RhB removal.

6. Conclusions and Perspectives

Ultrathin 2D materials and their hybridizations with the maintenance of 2D configuration are excellent candidates for fundamental photocatalytic research and potential commercial applications. This comprehensive review highlights recent advances in the application of ultrathin 2D materials towards photocatalytic solar energy conversion. First, this review presents a thoroughly summary of the classification, controllable synthesis and formation mechanism of ultrathin 2D photocatalysts. Then, strategies to tune the electronic structure of ultrathin 2D materials and further impact the photocatalytic properties are summarized, namely component tuning, thickness tuning, doping and defect engineering. Moreover, further hybridizations with the maintaining of ultrathin 2D feature has been presented to further boost the photocatalytic behaviors, including quantum dot/2D materials, single atom/2D materials, molecular/2D materials, and 2D-2D stacking materials. Finally, various photocatalytic applications over ultrathin 2D photocatalysts have been surveyed with the emphasis of structure-performance relationship insights, including water oxidation, hydrogen evolution, CO_2 reduction, nitrogen fixation, organic syntheses, and pollutants removal.

Despite considerable progress in the ultrathin 2D materials towards photocatalysis, it still faces a large amount of challenges in this area. Firstly, apart from the widely developed ultrathin 2D materials such as metal oxides, hydroxides and sulfides for photocatalytic processes, other types of potential ultrathin 2D materials with novel structural features or electronic properties towards photocatalysis should be explored, for example, the layered oxyhalides (such as FeOBr, Bi_4VO_8Cl), thiophosphates (such as $CoPS_3$), multi-metal chalcogenides (such as Cu_2ZnGeS_4) or metal-free semiconductors (such as C_2N and C_3N). Especially, the ultrathin 2D materials with intrinsic non-van der Waals layered structure hold great potential in photocatalysis, owing to the abundant surface atoms with dangling bonds afford high active to build excellent chemical environment for promoting chemisorptions of reaction molecular and boost the catalytic reaction dynamics. Secondly, there have rare scalable strategies to yield the ultrathin 2D photocatalysts in large-scale with controllable thickness or atomic structures. The large quantity manufacture of ultrathin 2D photocatalysts is of great importance for the potential commercial applications and thus more attentions should be paid on the approaches of low cost large scale production. Thirdly, the atomic-scale thickness allow the ultrathin materials with easily adjustable electronic structures, which shows significantly impact on the photocatalytic behavior. Apart from element doping, defect engineering etc., other effective strategies such as tuning surface state or surface atom tensile strains, should be developed to tune the electronic structure and thus extreme promote the photocatalytic performance. Fourthly, the ultrathin 2D configuration supply an ideal material model to discriminate catalytically active site and further tune type and quantity of reaction centers to meet the specific catalytic process. However, the explorations focused to the mechanism of photocatalysis is still inadequately. More efforts should be dedicated to optimize theoretical calculation conditions with closer to realistic reaction systems. The synergistic utilization of theoretical calculations with advanced *in situ* characterizations can help to deepen insights into the correlation between local atomic microstructure and activity and clarify the reaction processes. Fifthly, owing to the respective weakness of each materials, a desired approach to

acquire the optimal properties is to perform the assembling of different building blocks to create cooperative effect. It is believed that this comprehensive review will contribute to the further researches in the area of ultrathin 2D materials or photocatalysis.

Acknowledgements

J. Di and J. Xiong contributed equally to this work. This work was financially supported by the National Natural Science Foundation of China (No. 21476098, 21606113 and 21676128), Singapore National Research Foundation (NRF RF Award No. NRF-RF2013-08), MOE Tier 2 grant MOE2016-T2-1-131 (S), Doctoral Innovation Fund of Jiangsu Province (KYZZ16_0340) and China Scholarship Council.

Received: ((will be filled in by the editorial staff))
Revised: ((will be filled in by the editorial staff))
Published online: ((will be filled in by the editorial staff))

References

[1] H. T. Wang, H. T. Yuan, S. S. Hong, Y. B. Li, Y. Cui, *Chem. Soc. Rev.* **2015**, *44*, 2664.

[2] F. Bonaccorso, L. Colombo, G. H. Yu, M. Stoller, V. Tozzini, A. C. Ferrari, R. S. Ruoff, V. Pellegrini, *Science* **2015**, *347*, 1246501.

[3] M. Nasilowski, B. Mahler, E. Lhuillier, S. Ithurria, B. Dubertret, *Chem. Rev.* **2016**, *116*, 10934.

[4] C. L. Tan, H. Zhang, *Nat. Commun.* **2015**, *6*, 7873.

[5] C. L. Tan, X. H. Cao, X. J. Wu, Q. Y. He, J. Yang, X. Zhang, J. Z. Chen, W. Zhao, S. K. Han, G. H. Nam, M. Sindoro, H. Zhang, *Chem. Rev.* **2017**, *117*, 6225.

[6] Y. Q. Guo, K. Xu, C. Z. Wu, J. Y. Zhao, Y. Xie, *Chem. Soc. Rev.* **2015**, *44*, 637.

[7] D. H. Deng, K. S. Novoselov, Q. Fu, N. F. Zheng, Z. Q. Tian, X. H. Bao, *Nat. Nanotechnol.* **2016**, *11*, 218.

[8] Y. F. Sun, S. Gao, F. C. Lei, C. Xiao, Y. Xie, *Acc. Chem. Res.* **2015**, *48*, 3.

[9] X. D. Zhang, Y. Xie, *Chem. Soc. Rev.* **2013**, *42*, 8187.

[10] J. R. Ran, J. Zhang, J. G. Yu, M. Jaroniec, S. Z. Qiao, *Chem. Soc. Rev.* **2014**, *43*, 7787.

[11] Q. J. Xiang, B. Cheng, J. G. Yu, *Angew. Chem. Int. Ed.* **2015**, *54*, 11350.

[12] P. Li, Y. Zhou, Z. Y. Zhao, Q. F. Xu, X. Y. Wang, M. Xiao, Z. G. Zou, *J. Am. Chem. Soc.* **2015**, *137*, 9547.

[13] M. Q. Yang, N. Zhang, M. Pagliaro, Y. J. Xu, *Chem. Soc. Rev.* **2014**, *43*, 8240.

[14] J. Di, J. X. Xia, H. M. Li, Z. Liu, *Nano Energy* **2017**, *35*, 79.

[15] G. S. Li, Z. C. Lian, W. C. Wang, D. Q. Zhang, H. X. Li, *Nano Energy* **2016**, *19*, 446.

[16] J. Li, H. Li, G. M. Zhan, L. Z. Zhang, *Acc. Chem. Res.* **2017**, *50*, 112.

[17] J. Di, J. X. Xia, Y. P. Ge, H. P. Li, H. Y. Ji, H. Xu, Q. Zhang, H. M. Li, M. N. Li, *Appl. Catal. B* **2015**, *168-169*, 51.

[18] Y. Ma, X. L. Wang, Y. S. Jia, X. B. Chen, H. X. Han, C. Li, *Chem. Rev.* **2014**, *114*, 9987.

[19] X. X. Chang, T. Wang, J. L. Gong, *Energy Environ. Sci.* **2016**, *9*, 2177.

[20] Y. F. Sun, S. Gao, F. C. Lei, Y. Xie, *Chem. Soc. Rev.* **2015**, *44*, 623.

[21] J. S. Zhang, Y. Chen, X. C. Wang, *Energy Environ. Sci.* **2015**, *8*, 3092.

[22] B. Luo, G. Liu, L. Z. Wang, *Nanoscale* **2016**, *8*, 6904.

[23] S. Ida, T. Ishihara, *J. Phys. Chem. Lett.* **2014**, *5*, 2533.

[24] S. Qamar, F. C. Lei, L. Liang, S. Gao, K. T. Liu, Y. F. Sun, W. X. Ni, Y. Xie, *Nano Energy* **2016**, *26*, 692.

[25] J. Yang, Y. L. Jiang, L. J. Li, E. Muhire, M. Z. Gao, *Nanoscale* **2016**, *8*, 8170.

[26] D. Liu, Y. H. Lv, M. Zhang, Y. F. Liu, Y. Y. Zhu, R. L. Zong, Y. F. Zhu, *J. Mater. Chem. A* **2014**, *2*, 15377.

[27] Y. W. Liu, L. Liang, C. Xiao, X. M. Hua, Z. Li, B. C. Pan, Y. Xie, *Adv. Energy Mater.* **2016**, 1600437.

[28] X. Y. Chen, Y. Zhou, Q. Liu, Z. D. Li, J. G. Liu, Z. G. Zou, *ACS Appl. Mater. Interfaces* **2012**, *4*, 3372.

[29] M. R. Waller, T. K. Townsend, J. Zhao, E. M. Sabio, R. L. Chamousis, N. D. Browning, F. E. Osterloh, *Chem. Mater.* **2012**, *24*, 698.

[30] J. X. Zhu, Z. Y. Yin, D. Yang, T. Sun, H. Yu, H. E. Hoster, H. H. Hng, H. Zhang, Q. Y. Yan, *Energy Environ. Sci.* **2013**, *6*, 987.

[31] S. Gao, Y. F. Sun, F. C. Lei, J. W. Liu, L. Liang, T. W. Li, B. C. Pan, J. F. Zhou, Y. Xie, *Nano Energy* **2014**, *8*, 205.

[32] L. Liang, Y. F. Sun, F. C. Lei, S. Gao, Y. Xie, *J. Mater. Chem. A* **2014**, *2*, 10647.

[33] Y. F. Yu, Y. M. Zhu, M. Meng, *Dalton Trans.* **2013**, *42*, 12087.

[34] F. C. Lei, Y. F. Sun, K. T. Liu, S. Gao, L. Liang, B. C. Pan, Y. Xie, *J. Am. Chem. Soc.* **2014**, *136*, 6826.

[35] J. H. Xiong, L. R. Wen, F. Jiang, Y. H. Liu, S. J. Liang, L. Wu, *J. Mater. Chem. A* **2015**, *3*, 20627.

[36] Z. Q. Sun, T. Liao, Y. H. Dou, S. M. Hwang, M. S. Park, L. Jiang, J. H. Kim, S. X. Dou, *Nat. Commun.* **2014**, *5*, 3813.

[37] K. Maeda, M. Eguchi, T. Oshima, *Angew. Chem. Int. Ed.* **2014**, *53*, 13164.

[38] S. Park, H. J. Song, C. W. Lee, S. W. Hwang, I. S. Cho, *ACS Appl. Mater. Interfaces* **2015**, *7*, 21860.

[39] Y. H. Liu, J. H. Xiong, S. G. Luo, R. W. Liang, N. Qin, S. J. Liang, L. Wu, *Chem. Commun.* **2015**, *51*, 15125.

[40] C. Zhou, Y. F. Zhao, L. Shang, R. Shi, L. Z. Wu, C. H. Tung, T. R. Zhang, *Chem. Commun.* **2016**, *52*, 8239.

[41] H. J. Yin, Z. Y. Tang, *Chem. Soc. Rev.* **2016**, *45*, 4873.

[42] Y. F. Zhao, X. D. Jia, G. I. N. Waterhouse, L. Z. Wu, C. H. Tung, D. O'Hare, T. R. Zhang, *Adv. Energy Mater.* **2016**, *6*, 1501974.

[43] Y. F. Zhao, G. B. Chen, T. Bian, C. Zhou, G. I. N. Waterhouse, L. Z. Wu, C. H. Tung, L. J. Smith, D. O'Hare, T. R. Zhang, *Adv. Mater.* **2015**, *27*, 7824.

[44] S. He, Y. Y. Huang, J. H. Huang, W. Liu, T. Yao, S. Jiang, F. M. Tang, J. K. Liu, F. C. Hu, Z. Y. Pan, Q. H. Liu, *J. Phys. Chem. C* **2015**, *119*, 26362.

[45] Y. F. Zhao, B. Li, Q. Wang, W. Gao, C. L. J. Wang, M. Wei, D. G. Evans, X. Duan, D. O'Hare, *Chem. Sci.* **2014**, *5*, 951.

[46] Y. F. Zhao, C. L. J. Wang, W. Gao, B. Li, Q. Wang, L. R. Zheng, M. Wei, D. G. Evans, X. Duan, D. O'Hare, *J. Mater. Chem. B* **2013**, *1*, 5988.

[47] Y. Xu, W. W. Zhao, R. Xu, Y. M. Shi, B. Zhang, *Chem. Commun.* **2013**, *49*, 9803.

[48] M. Zhukovskyi, P. Tongying, H. Yashan, Y. X. Wang, M. Kuno, *ACS Catal.* **2015**, *5*, 6615-6623.

[49] S. M. Sun, X. M. Li, W. Z. Wang, L. Zhang, X. Sun, *Appl. Catal. B* **2017**, *200*, 323.

[50] Y. F. Sun, Z. H. Sun, S. Gao, H. Cheng, Q. H. Liu, F. C. Lei, S. Q. Wei, Y. Xie, *Adv. Energy Mater.* **2014**, *4*, 1300611.

[51] Y. F. Sun, H. Cheng, S. Gao, Z. H. Sun, Q. H. Liu, Q. Liu, F. C. Lei, T. Yao, J. F. He, S. Q. Wei, Y. Xie, *Angew. Chem. Int. Ed.* **2012**, *51*, 8727.

[52] F. C. Lei, L. Zhang, Y. F. Sun, L. Liang, K. T. Liu, J. Q. Xu, Q. Zhang, B. C. Pan, Y. Luo, Y. Xie, *Angew. Chem. Int. Ed.* **2015**, *54*, 9266.

[53] W. L. Yang, L. Zhang, J. F. Xie, X. D. Zhang, Q. H. Liu, T. Yao, S. Q. Wei, Q. Zhang, Y. Xie, *Angew. Chem. Int. Ed.* **2016**, *55*, 6716.

[54] P. Hu, C. K. Ngaw, Y. P. Yuan, P. S. Bassi, S. C. J. Loo, T. T. Y. Tan, *Nano Energy* **2016**, *26*, 577.

[55] Y. F. Sun, Z. H. Sun, S. Gao, H. Cheng, Q. H. Liu, J. Y. Piao, T. Yao, C. Z. Wu, S. L. Hu, S. Q. Wei, Y. Xie, *Nat. Commun.* **2012**, *3*, 1057.

[56] Y. G. Zhou, Y. F. Zhang, M. S. Lin, J. L. Long, Z. Z. Zhang, H. X. Lin, J. C.-S. Wu, X. X. Wang, *Nat. Commun.* **2015**, *6*, 8340.

[57] L. Liang, F. C. Lei, S. Gao, Y. F. Sun, X. C. Jiao, J. Wu, S. Qamar, Y. Xie, *Angew. Chem. Int. Ed.* **2015**, *54*, 13971.

[58] J. G. Hou, S. Y. Cao, Y. Z. Wu, F. Liang, Y. F. Sun, Z. S. Lin, L. C. Sun, *Nano Energy* **2017**, *32*, 359.

[59] J. Di, J. X. Xia, M. X. Ji, H. P. Li, H. Xu, H. M. Li, R. Chen, *Nanoscale* **2015**, *7*, 11433.

[60] S. Gao, B. C. Gu, X. C. Jiao, Y. F. Sun, X. L. Zu, F. Yang, W. G. Zhu, C. M. Wang, Z. M. Feng, B. J. Ye, Y. Xie, *J. Am. Chem. Soc.* **2017**, *139*, 3438.

[61] J. Di, J. X. Xia, Y. Huang, M. X. Ji, W. M. Fan, Z. G. Chen, H. M. Li, *Chem. Eng. J.* **2016**, *302*, 334.

[62] Q. Q. Wang, L. P. Yuan, M. Dun, X. M. Yang, H. Chen, J. L. Li, J. C. Hu, *Appl. Catal. B* **2016**, *196*, 127.

[63] M. L. Guan, C. Xiao, J. Zhang, S. J. Fan, R. An, Q. M. Cheng, J. F. Xie, M. Zhou, B. J. Ye, Y. Xie, *J. Am. Chem. Soc.* **2013**, *135*, 10411.

[64] J. Chen, M. L. Guan, W. Z. Cai, J. J. Guo, C. Xiao, G. K. Zhang, *Phys. Chem. Chem. Phys.* **2014**, *16*, 20909.

[65] J. Di, J. X. Xia, M. X. Ji, B. Wang, S. Yin, Q. Zhang, Z. G. Chen, H. M. Li, *ACS Appl. Mater. Interfaces* **2015**, *7*, 20111.

[66] J. Di, J. X. Xia, M. X. Ji, L. Xu, S. Yin, Z. G. Chen, H. M. Li, *J. Mater. Chem. A* **2016**, *4*, 5051.

[67] L. Zhang, Z. K. Han, W. Z. Wang, X. M. Li, Y. Su, D. Jiang, X. L. Lei, S. M. Sun, *Chem. Eur. J.* **2015**, *21*, 18089.

[68] Y. Mi, L. Y. Wen, Z. J. Wang, D. W. Cao, R. Xu, Y. G. Fang, Y. L. Zhou, Y. Lei, *Nano Energy* **2016**, *30*, 109.

[69] P. Niu, L. L. Zhang, G. Liu, H. M. Cheng, *Adv. Funct. Mater.* **2012**, *22*, 4763.

[70] J. Di, J. X. Xia, X. W. Li, M. X. Ji, H. Xu, Z. G. Chen, H. M. Li, *Carbon* **2016**, *107*, 1.

[71] H. Xu, J. Yan, X. J. She, L. Xu, J. X. Xia, Y. G. Xu, Y. H. Song, L. Y. Huang, H. M. Li, *Nanoscale* **2014**, *6*, 1406.

[72] Y. F. Li, R. X. Jin, Y. Xing, J. Q. Li, S. Y. Song, X. C. Liu, M. Li, R. C. Jin, *Adv. Energy Mater.* **2016**, 1601273.

[73] X. J. She, J. J. Wu, J. Zhong, H. Xu, Y. C. Yang, R. Vajtai, J. Lou, Y. Liu, D. L. Du, H. M. Li, P. M. Ajayan, *Nano Energy* **2016**, *27*, 138.

[74] X. D. Zhang, X. Xie, H. Wang, J. J. Zhang, B. C. Pan, Y. Xie, *J. Am. Chem. Soc.* **2013**, *135*, 18.

[75] S. B. Yang, Y. J. Gong, J. S. Zhang, L. Zhan, L. L. Ma, Z. Y. Fang, R. Vajtai, X. C. Wang, P. M. Ajayan, *Adv. Mater.* **2013**, *25*, 2452.

[76] Q. Y. Lin, L. Li, S. J. Liang, M. H. Liu, J. H. Bi, L. Wu, *Appl. Catal. B* **2015**, *163*, 135.

[77] H. H. Ou, L. H. Lin, Y. Zheng, P. J. Yang, Y. X. Fang, X. C. Wang, *Adv. Mater.* **2017**, *29*, 1700008.

[78] H. Wang, X. Z. Yang, W. Shao, S. C. Chen, J. F. Xie, X. D. Zhang, J. Wang, Y. Xie, *J. Am. Chem. Soc.* **2015**, *137*, 11376.

[79] J. Ryu, Y. J. Jang, S. Choi, H. J. Kang, H. Park, J. S. Lee, S. Park, *NPG Asia Mater.* **2016**, *8*, e248.

[80] S. Li, H. Wang, D. D. Li, X. D. Zhang, Y. F. Wang, J. F. Xie, J. Y. Wang, Y. P. Tian, W. X. Ni, Y. Xie, *J. Mater. Chem. A* **2016**, *4*, 15841.

[81] J. Li, G. M. Zhan, Y. Yu, L. Z. Zhang, *Nat. Commun.* **2016**, *7*, 11480.

[82] J. Di, J. X. Xia, M. X. Ji, S. Yin, H. P. Li, H. Xu, Q. Zhang, H. M. Li, *J. Mater. Chem. A* **2015**, *3*, 15108.

[83] L. Q. Ye, X. L. Jin, C. Liu, C. H. Ding, H. Q. Xie, K. H. Chu, P. K. Wong, *Appl. Catal. B* **2016**, *187*, 281.

[84] Y. Bai, T. Chen, P. Q. Wang, L. Wang, L. Q. Ye, *Chem. Eng. J.* **2016**, *304*, 454.

[85] J. X. Xia, M. X. Ji, J. Di, B. Wang, S. Yin, M. Q. He, Q. Zhang, H. M. Li, *J. Alloy. Compd.* **2017**, *695*, 922.

[86] Y. Okamoto, S. Ida, J. Hyodo, H. Hagiwara, T. Ishihara, *J. Am. Chem. Soc.* **2011**, *133*, 18034.

[87] Z. W. Chen, X. Y. Jiang, C. B. Zhu, C. K. Shi, *Appl. Catal. B* **2016**, *199*, 241.

[88] J. H. Xiong, Y. H. Liu, S. J. Liang, S. Y. Zhang, Y. H. Li, L. Wu, *J. Catal.* **2016**, *342*, 98.

[89] Y. R. Li, Z. W. Wang, T. Xia, H. X. Ju, K. Zhang, R. Long, Q. Xu, C. M. Wang, L. Song, J. F. Zhu, J. Jiang, Y. J. Xiong, *Adv. Mater.* **2016**, *28*, 6959.

[90] G. Liu, P. Niu, C. H. Sun, S. C. Smith, Z. G. Chen, G. Q. Lu, H. M. Cheng, *J. Am. Chem. Soc.* **2010**, *132*, 11642.

[91] Z. Z. Lin, X. C.Wang, *Angew. Chem. Int. Ed.* **2013**, *52*, 1735.

[92] H. Wang, X. D. Zhang, J. F. Xie, J. J. Zhang, P. Ma, B. C. Pan, Y. Xie, *Nanoscale* **2015**, *7*, 5152.

[93] C. J. Huang, C. Chen, M. W. Zhang, L. H. Lin, X. X. Ye, S. Lin, M. Antonietti, X. C. Wang, *Nat. Commun.* **2015**, *6*, 7698.

[94] Y. W. Liu, C. Xiao, Z. Li, Y. Xie, *Adv. Energy Mater.* **2016**, *6*, 1600436.

[95] W. T. Bi, C. M. Ye, C. Xiao, W. Tong, X. D. Zhang, W. Shao, Y. Xie, *Small* **2014**, *10*, 2820.

[96] Q. H. Liang, Z. Li, Z. H. Huang, F. Y. Kang, Q. H. Yang, *Adv. Funct. Mater.* **2015**, *25*, 6885.

[97] J. Di, J. X. Xia, M. X. Ji, B. Wang, S. Yin, Y. Huang, Z. G. Chen, H. M. Li, *Appl. Catal. B* **2016**, *188*, 376.

[98] J. Liu, Y. Liu, N. Y. Liu, Y. Z. Han, X. Zhang, H. Huang, Y. Lifshitz, S. T. Lee, J. Zhong, Z. H. Kang, *Science* **2015**, *347*, 970.

[99] J. X. Xia, J. Di, H. T. Li, H. Xu, H. M. Li, S. J. Guo, *Appl. Catal. B* **2016**, *181*, 260.

[100] X. Y. Liu, H. Chen, R. L. Wang, Y. Q. Shang, Q. Zhang, W. Li, G. Z. Zhang, J. Su, C. T. Dinh, F. P. G. Arquer, J. Li, J. Jiang, Q. X. Mi, R. Si, X. P. Li, Y. H. Sun, Y. T. Long, H. Tian, E. H. Sargent, Z. J. Ning, *Adv. Mater.* **2017**, 1605646.

[101] Y. F. Ji, W. Guo, H. H. Chen, L. S. Zhang, S. Chen, M. T. Hua, Y. H. Long, Z. Chen, *J. Phys. Chem. C* **2015**, *119*, 27053.

[102] Y. T. Lu, D. M. Chu, M. S. Zhu, Y. K. Du, P. Yang, *Phys. Chem. Chem. Phys.* **2015**, *17*, 17355.

[103] J. Y. Liu, *ACS Catal.* **2017**, *7*, 34.

[104] B. T. Qiao, A. Q. Wang, X. F. Yang, L. F. Allard, Z. Jiang, Y. T. Cui, J. Y. Liu, J. Li, T. Zhang, *Nat. Chem.* **2011**, *3*, 634.

[105] Z. P. Chen, S. Pronkin, T. P. Fellinger, K. Kailasam, G. Vilé, D. Albani, F. Krumeich, R. Leary, J. Barnard, J. M. Thomas, J. Pérez-Ramírez, M. Antonietti, D. Dontsova, *ACS Nano* **2016**, *10*, 3166.

[106] X. G. Li, W. T. Bi, L. Zhang, S. Tao, W. S. Chu, Q. Zhang, Y. Luo, C. Z. Wu, Y. Xie, *Adv. Mater.* **2016**, *28*, 2427.

[107] S. Ida, N. Kim, E. Ertekin, S. Takenaka, T. Ishihara, *J. Am. Chem. Soc.* **2015**, *137*, 239.

[108] Z. J. Han, F. Qiu, R. Eisenberg, P. L. Holland, T. D. Krauss, *Science* **2012**, *338*, 1321.

[109] Y. Xu, X. G. Yin, Y. Huang, P. W. Du, B. Zhang, *Chem. Eur. J.* **2015**, *21*, 4571.

[110] X. L. Lu, K. Xu, S. Tao, Z. W. Shao, X. Peng, W. T. Bi, P. Z. Chen, H. Ding, W. S. Chu, C. Z. Wu, Y. Xie, *Chem. Sci.* **2016**, *7*, 1462.

[111] W. T. Bi, X. G. Li, L. Zhang, T. Jin, L. D. Zhang, Q. Zhang, Y. Luo, C. Z. Wu, Y. Xie, *Nat. Commun.* **2015**, *6*, 8647.

[112]. S. Ida, A. Takashiba, S. Koga, H. Hagiwara, T. Ishihara, *J. Am. Chem. Soc.* **2014**, *136*, 1872.

[113] Y. J. Yuan, Z. J. Ye, H. W. Lu, B. Hu, Y. H. Li, D. Q. Chen, J. S. Zhong, Z. T. Yu, Z. G. Zou, *ACS Catal.* **2016**, *6*, 532.

[114] J. Z. Chen, X. J. Wu, L. S. Yin, B. Li, X. Hong, Z. X. Fan, B. Chen, C. Xue, H. Zhang, *Angew. Chem. Int. Ed.* **2015**, *54*, 1210.

[115] Y. D. Hou, A. B. Laursen, J. S. Zhang, G. G. Zhang, Y. S. Zhu, X. C. Wang, S. Dahl, I. Chorkendorff, *Angew. Chem. Int. Ed.* **2013**, *52*, 3621.

[116] Z. Y. Zhang, J. D. Huang, M. Y. Zhang, Q. Yuan, B. Dong, *Appl. Catal. B* **2015**, *163*, 298.

[117] X. J. She, J. J. Wu, H. Xu, J. Zhong, Y. Wang, Y. H. Song, K. Q. Nie, Y. Liu, Y. C. Yang, M. T. F. Rodrigues, R. Vajtai, J. Lou, D. L. Du, H. M. Li, P. M. Ajayan, *Adv. Energy Mater.* **2017**, 1700025.

[118] J. X. Xia, M. X. Ji, J. Di, B. Wang, S. Yin, Q. Zhang, M. Q. He, H. M. Li, *Appl. Catal. B* **2016**, *191*, 235.

[119] J. L. Gunjakar, T. W. Kim, H. N. Kim, I. Y. Kim, S. J. Hwang, *J. Am. Chem. Soc.* **2011**, *133*, 14998.

[120] M. Q. Yang, Y. J. Xu, W. H. Lu, K. Y. Zeng, H. Zhu, Q. H. Xu, G. W. Ho, *Nat. Commun.* **2017**, *8*, 14224.

[121] J. Di, C. Chen, S. Z. Yang, M. X. Ji, C. Yan, K. Z. Gu, J. X. Xia, H. M. Li, S. Z. Li, Z. Liu, *J. Mater. Chem. A* **2017**, *5*, 14144.

[122] P. J. Yang, H. H. Ou, Y. X. Fang, X. C. Wang, *Angew. Chem. Int. Ed.* **2017**, *56*, 3992.

[123] X. C. Jiao, Z. W. Chen, X. D. Li, Y. F. Sun, S. Gao, W. S. Yan, C. M. Wang, Q. Zhang, Y. Lin, Y. Luo, Y. Xie, *J. Am. Chem. Soc.* **2017**, *139*, 7586.

[124] D. Zhu, L. H. Zhang, R. E. Ruther, R. J. Hamers, *Nat. Mater.* **2013**, *12*, 836.

[125] Y. Bai, L. Q. Ye, T. Chen, L. Wang, X. Shi, X. Zhang, D. Chen, *ACS Appl. Mater. Interfaces* **2016**, *8*, 27661.

[126] H. Li, J. Shang, Z. H. Ai, L. Z. Zhang, *J. Am. Chem. Soc.* **2015**, *137*, 6393.

[127] H. Li, F. Qin, Z. P. Yang, X. M. Cui, J. F. Wang, L. Z. Zhang, *J. Am. Chem. Soc.* **2017**, *139*, 3513.

[128] N. Zhang, X. Y. Li, H. C. Ye, S. M. Chen, H. X. Ju, D. B. Liu, Y. Lin, W. Ye, C. M. Wang, Q. Xu, J. F. Zhu, L. Song, J. Jiang, Y. J. Xiong, *J. Am. Chem. Soc.* **2016**, *138*, 8928.

[129] Y. H. Wu, B. Yuan, M. R. Li, W. H. Zhang, Y. Liu, C. Li, *Chem. Sci.* **2015**, *6*, 1873.

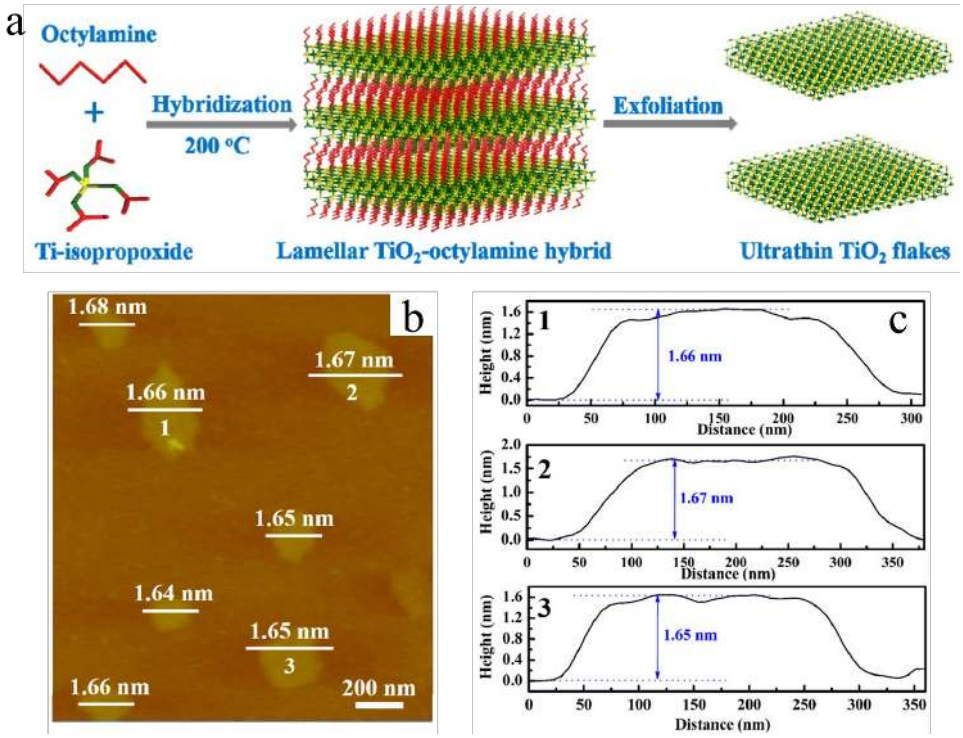

Figure 1. (a) Schematic illustration for the formation of ultrathin TiO_2 flakes, (b) AFM image of ultrathin TiO_2 flakes, (c) the height profiles corresponding to the AFM image in (b). Reproduced with permission.[24] 2016, Elsevier.

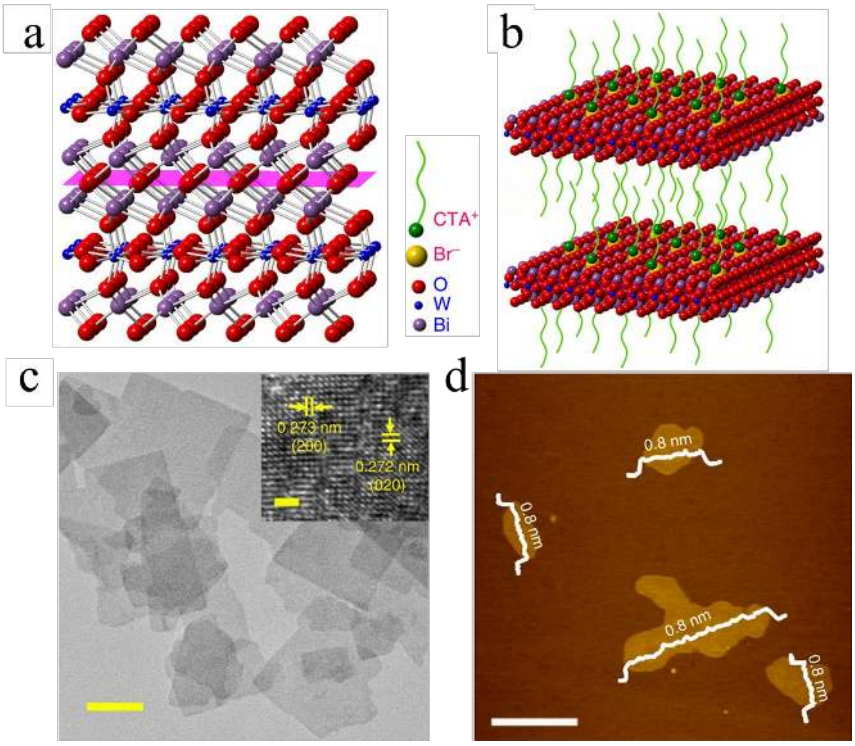

Figure 2. (a) Crystal structure of Bi_2WO_6, (b) Formation mechanism of the monolayer Bi_2WO_6 with CTAB assistance, (c) TEM image and the corresponding HRTEM image of the Bi_2WO_6 prepared with CTAB assistance, (d) AFM image of the monolayer Bi_2WO_6 prepared by CTAB assistance. Scale bar, 50 nm in c and 1 nm (insets in c), 500 nm in d. Reproduced with permission.[56] 2015, Nature Publishing Group.

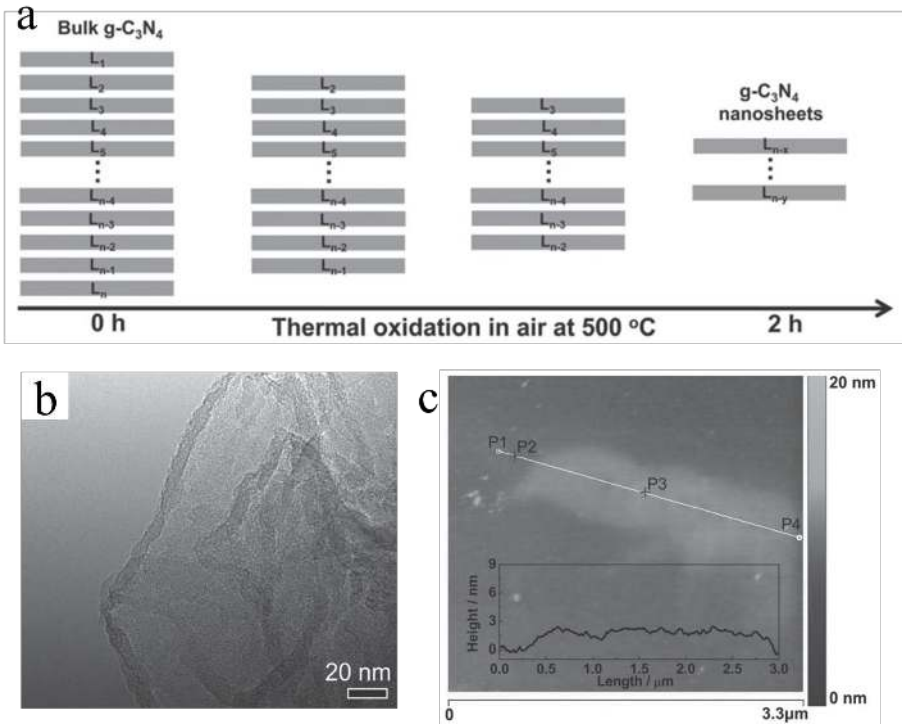

Figure 3. (a) Schematic of the formation process of the g-C_3N_4 nanosheets by thermal oxidation etching of bulk g-C_3N_4 at 500 ºC in air, (b) TEM image and (c) AFM image of g-C_3N_4 nanosheets. Reproduced with permission.[69] 2012, Wiley-VCH.

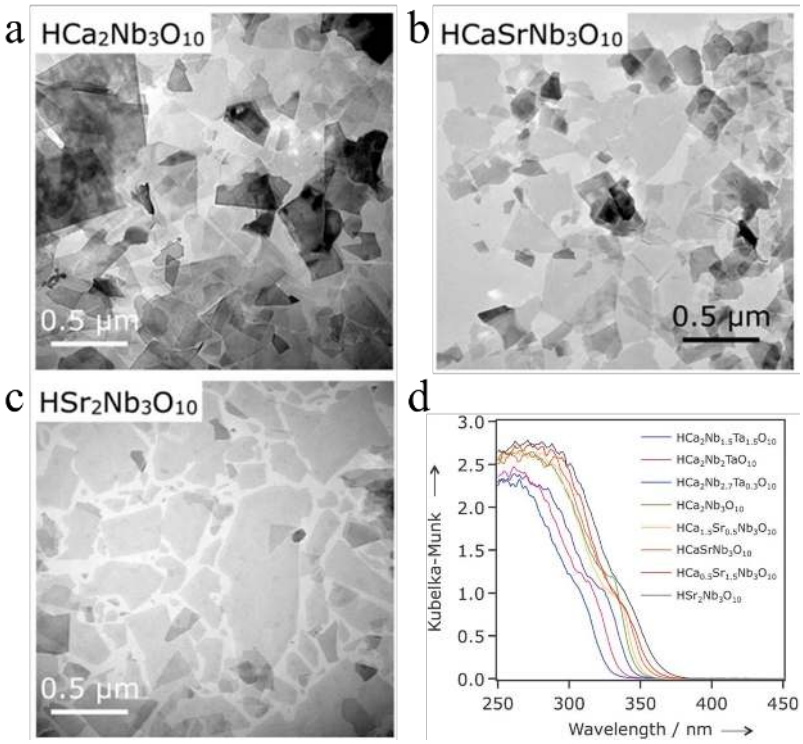

Figure 4. (a-c) Typical TEM images of TBA^+-exfoliated $Ca_{2-x}Sr_xNb_3O_{10}^-$ nanosheets, (d) UV/Vis diffuse reflectance spectra of restacked $HCa_{2-x}Sr_xNb_3O_{10}$ and $HCa_2Nb_{3-y}Ta_yO_{10}$ nanosheets. Reproduced with permission.[37] 2014, Wiley-VCH.

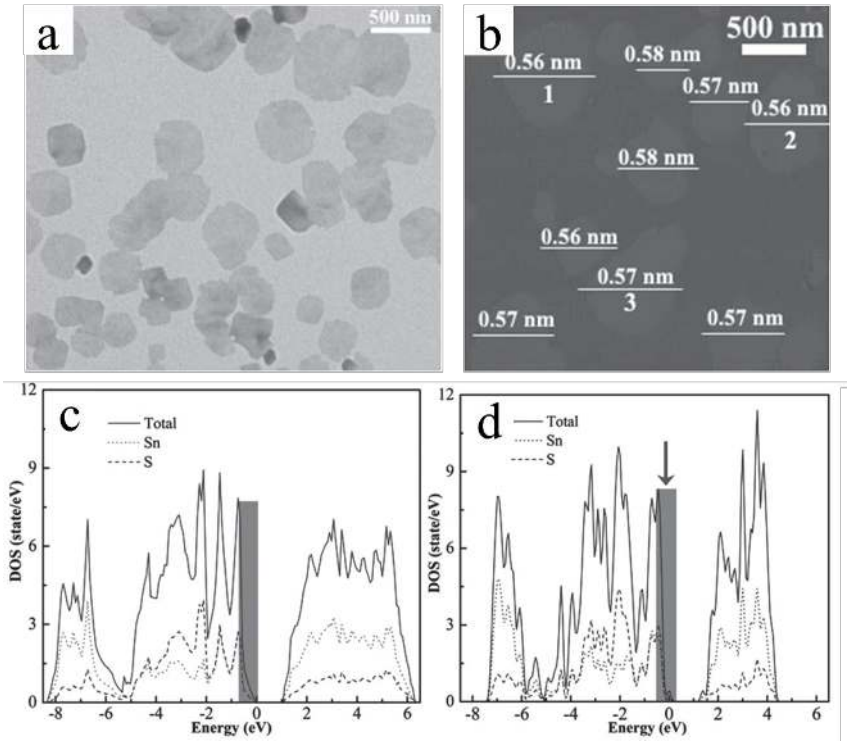

Figure 5. (a) TEM image and (b) AFM image of all-surface-atomic SnS sheets. Calculated density of states for (c) bulk SnS and (d) all-surface-atomic SnS monolayer. Reproduced with permission.[50] 2014, Wiley-VCH.

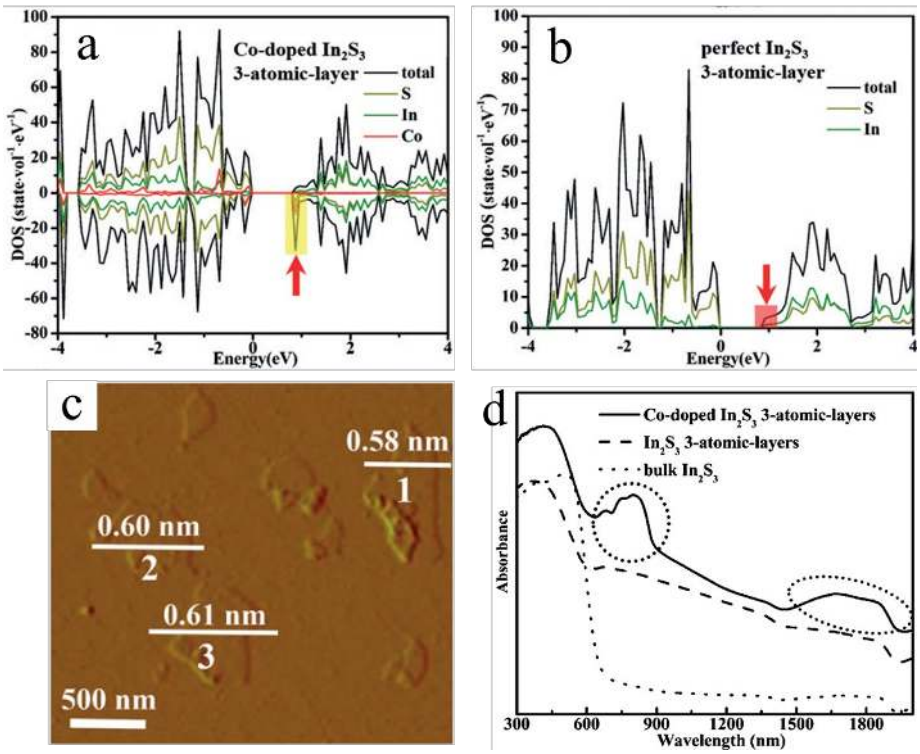

Figure 6. Calculated density of states of (a) Co-doped In_2S_3 three atomic layer slab, (b) perfect In_2S_3 three atomic layer slab. (c) AFM image of Co-doped In_2S_3, (d) UV/Vis diffuse reflectance spectra. Reproduced with permission.[52] 2015, Wiley-VCH.

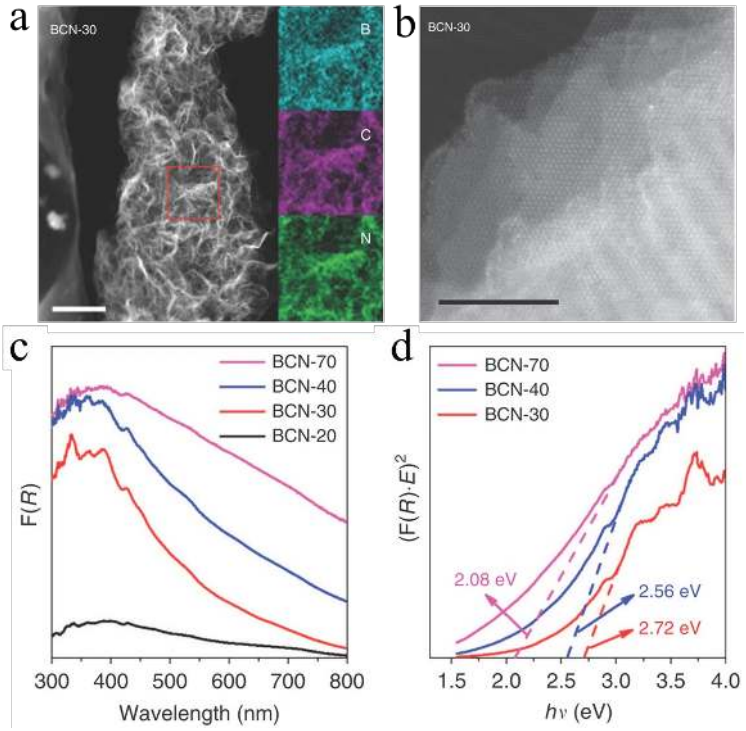

Figure 7. (a) Typical TEM dark-field image of BCN-30 sample and the elemental mapping images of B, C and N of the enlargement of selected-area in the picture. Scale bar, 300 nm. (b) High-resolution STEM of the BCN-30 sample along (002) facet. Scale bar, 5 nm. (c) ultraviolet-visible diffuse reflectance spectra (UV-vis DRS) of the BCN-x samples and (d) bandgap determination of the BCN-x samples from the $(F(R) \cdot E)^n$ versus E plots. Reproduced with permission.[93] 2015, Nature Publishing Group.

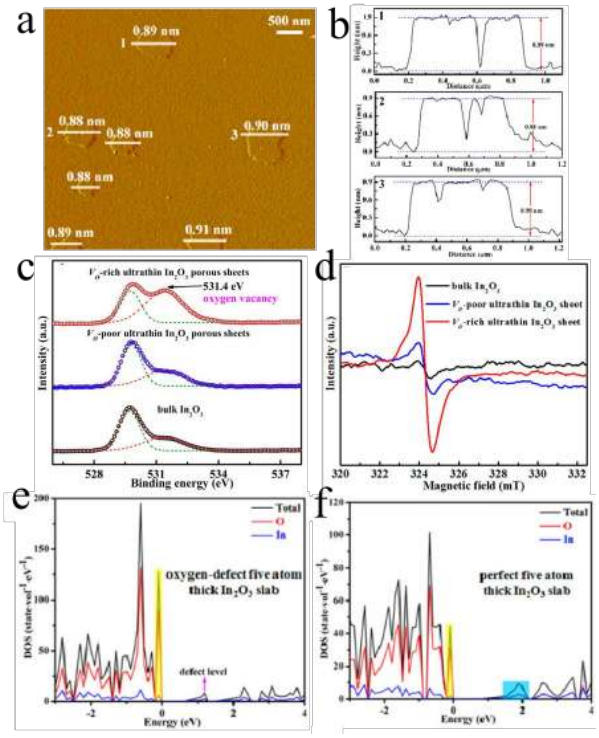

Figure 8. (a) AFM image, (b) the corresponding height profiles of V_O-rich atomically thin In_2O_3 porous sheets, (c) the O 1s XPS spectra, (d) electron spin resonance spectra. Calculated DOS of (e) oxygen-defect 5-atom-thick In_2O_3 slab, (f) perfect 5-atom-thick In_2O_3 slab. Reproduced with permission.[34] 2014, American Chemical Society.

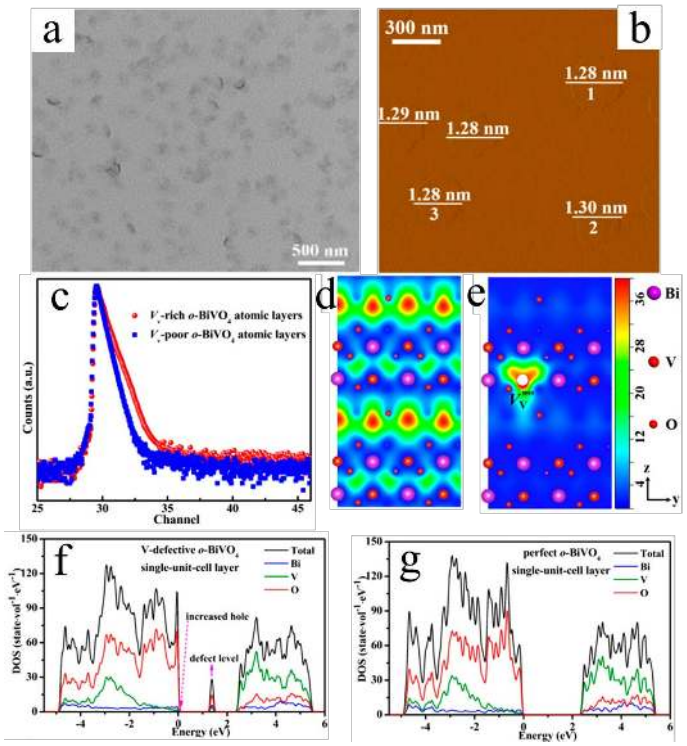

Figure 9. (a) TEM image, (b) AFM image of V_v-rich o-$BiVO_4$ atomic layers with one-unit-cell thickness. Defects characterization for the Vv-rich and Vv-poor o-$BiVO_4$ atomic layers: (c) Positron lifetime spectrum, (d, e) Schematic representation of trapped positrons. Calculated density of states of (f) V-defective o-$BiVO_4$ single-unit-cell layer slab and (g) perfect o-$BiVO_4$ single-unit-cell layer slab along the [001] orientation. Reproduced with permission.[60] 2017, American Chemical Society.

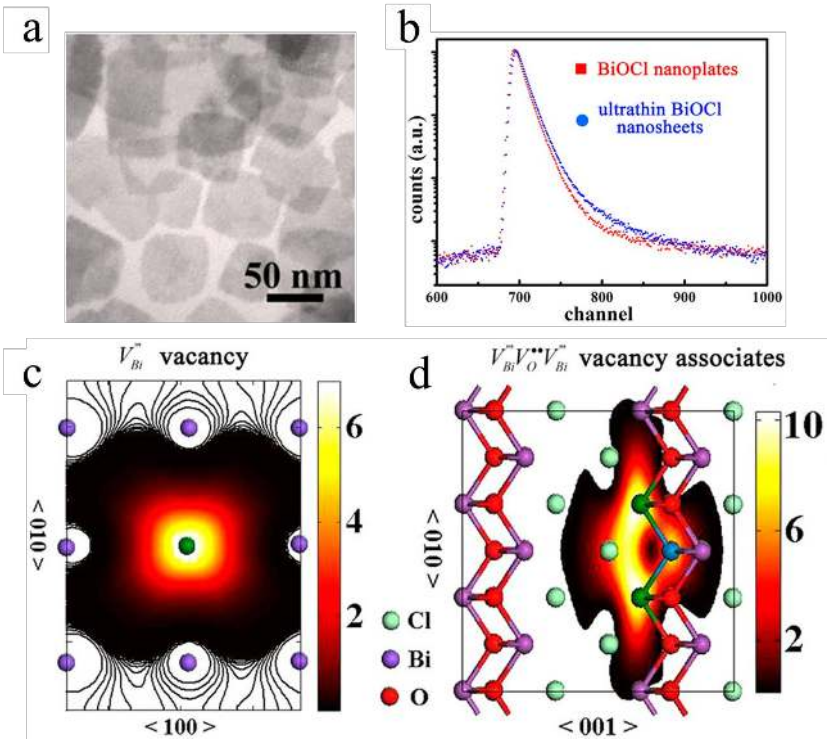

Figure 10. (a) TEM image of BiOCl ultrathin nanosheet. Positron annihilation spectroscopy of BiOCl ultrathin nanosheet and BiOCl nanoplates. (b) Positron lifetime spectrum of ultrathin BiOCl nanosheets and BiOCl nanoplates, respectively. (c, d) Schematic representations of trapped positrons of $V_{Bi}^{'''}$ defect and $V_{Bi}^{'''}V_O^{\cdot\cdot}V_{Bi}^{'''}$ vacancy associates, respectively. Reproduced with permission.[63] 2013, American Chemical Society.

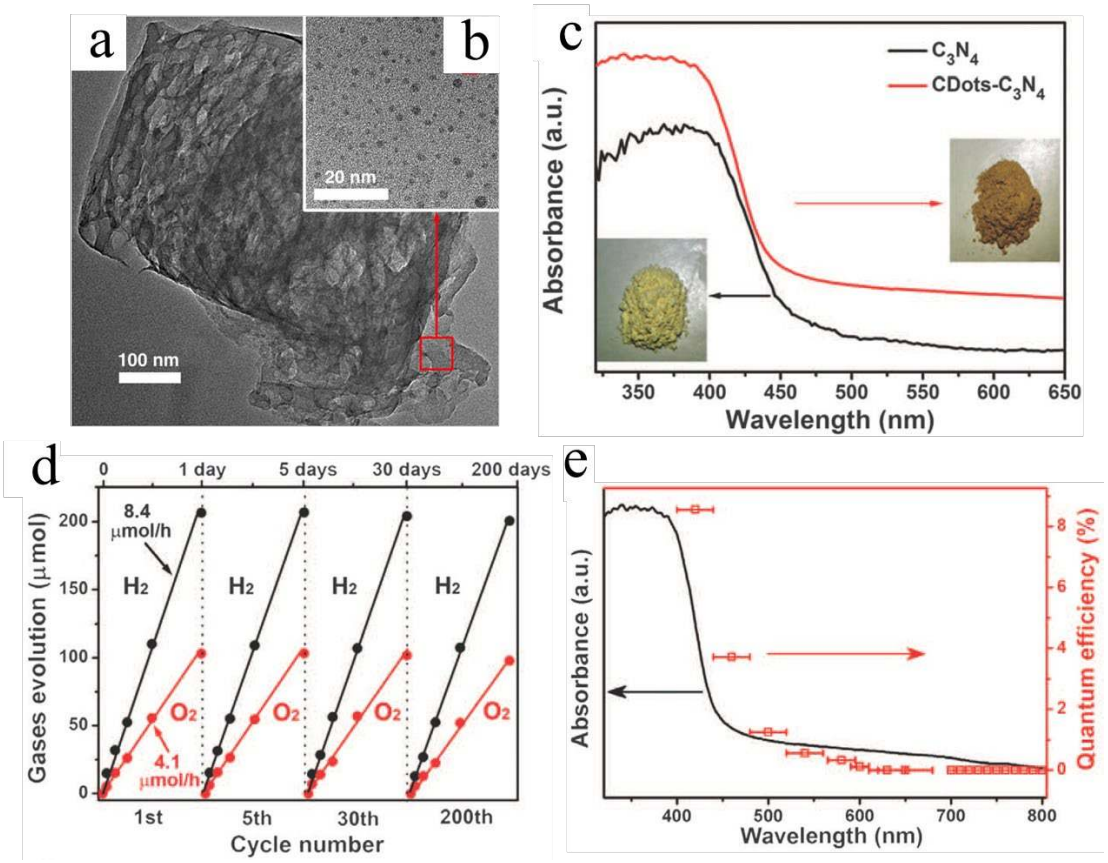

Figure 11. (a) TEM image of the CDots-C_3N_4 composite, (b) a magnified TEM image of the CDots-C_3N_4 region, (c) UV-vis absorption spectra of C_3N_4 and CDots-C_3N_4 catalysts, (d) typical time course of H_2 and O_2 production from water under visible light irradiation catalyzed by CDots-C_3N_4, (e) wavelength-dependent QE (red dots) of water splitting by CDots-C_3N_4. Reproduced with permission.[98] 2015, American Association for the Advancement of Science.

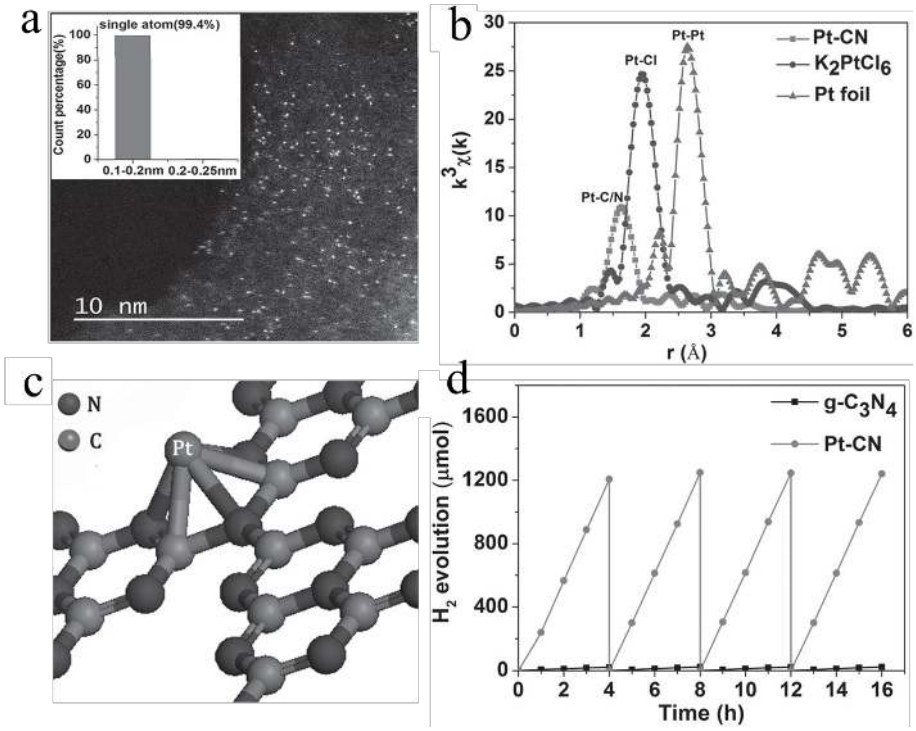

Figure 12. (a) HAADF-STEM image of Pt-CN. Inset is the size distribution of the bright spots, (b) Fourier transforms of the Pt L_3-edge EXAFS oscillations of Pt-CN, K_2PtCl_6, and Pt foil, (c) schematic models of Pt-CN, (d) Photocatalytic H_2 generation activity of g-C_3N_4 and Pt-CN. Reproduced with permission.[106] 2016, Wiley-VCH.

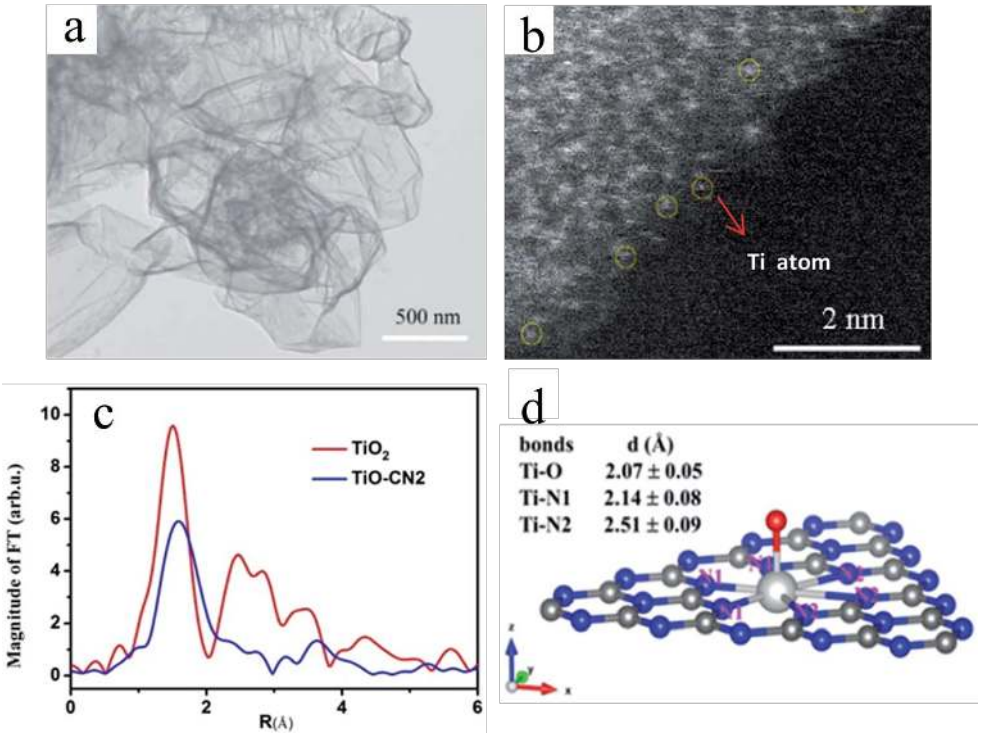

Figure 13. (a) TEM, (b) HAADF-STEM images of the TiO-CN2 nanosheet, (c) FT-EXAFS comparison between the prepared sample and standard anatase TiO_2, (d) the illustration of the detailed TiO-CN structure. Reproduced with permission.[110] 2016, Royal Society of Chemistry.

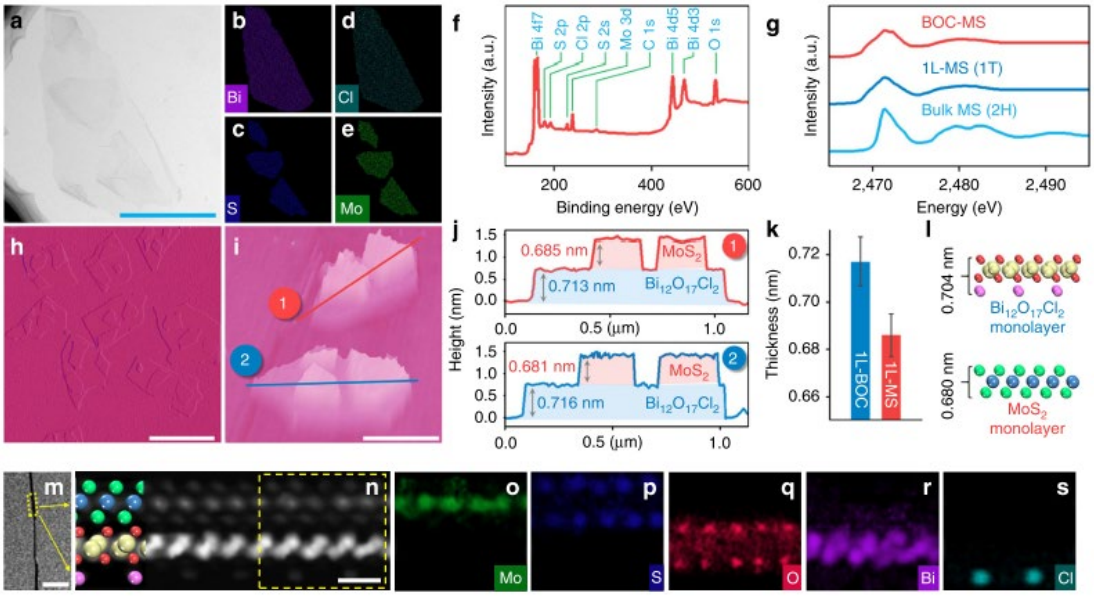

Figure 14. (a) Top-view TEM image, (b-e) elemental mapping images, (f) XPS spectra, (h,i) AFM images, side-view TEM image (m) and atomic-resolution HAADF-STEM image (n), and (o-s) the corresponding EELS elemental maps of BOC-MS. Scale bar, 500 nm, 1 mm, 500 nm, 10 nm and 5 Å, in a,h,i,m,n, respectively. (g) S K-edge XANES spectra of BOC-MS, 1L-MS and bulk MS. (j) Height profiles along the lines in i. (k) Comparison of the average thicknesses of 1L-BOC and 1L-MS in BOC-MS. The error bars in k represent the s.d. of over 100 independent AFM measurements. (l) The theoretical thicknesses of MoS_2 and $Bi_{12}O_{17}Cl_2$ monolayers. Reproduced with permission.[81] 2016, Nature Publishing Group.

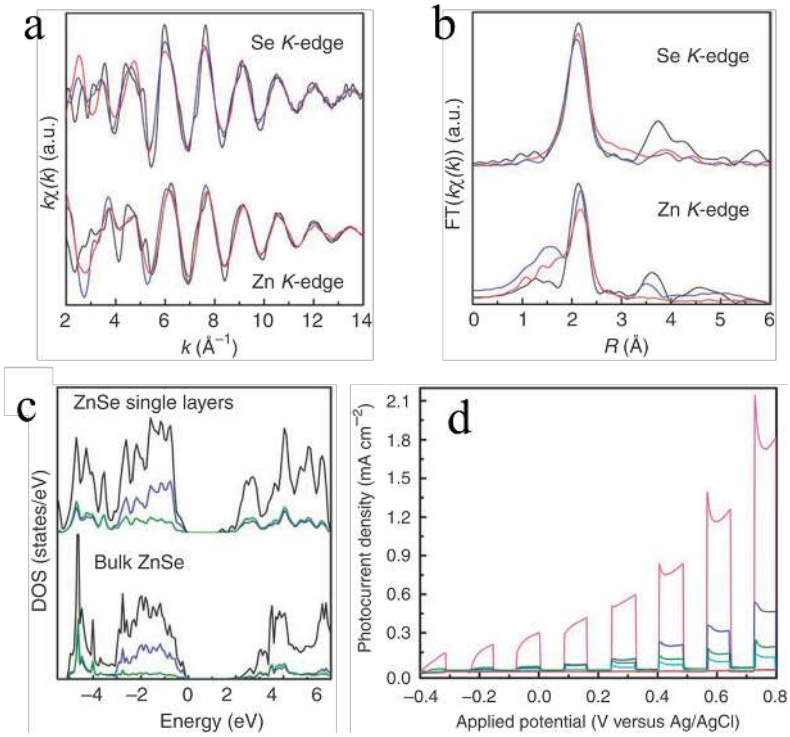

Figure 15. (a) Zn and Se K-edge extended XAFS oscillation function kχ(k) and (b) the corresponding Fourier transforms; the red, blue and black lines correspond to ZnSe single layers, ZnSe-pa single layers and bulk ZnSe, respectively, (c) the calculated DOS, the black, blue and olive lines denote the total, Se sp and Zn sp state density, respectively, (d) Photocurrent density versus applied potential curves under chopped 300 W Xe lamp irradiation. Reproduced with permission.[55] 2012, Nature Publishing Group.

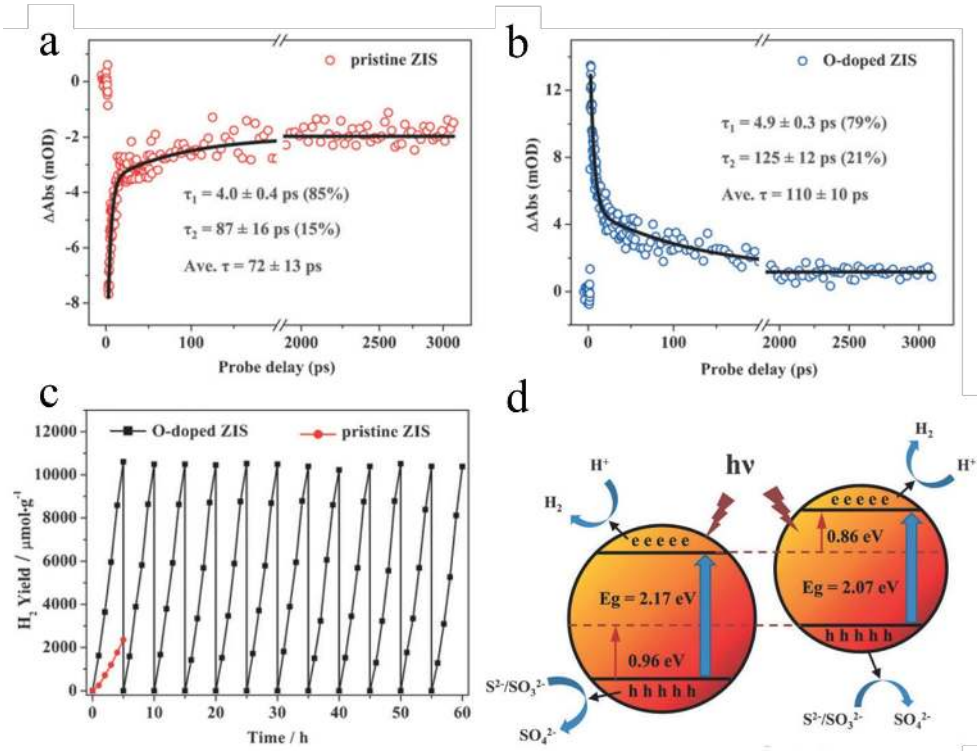

Figure 16. Ultrafast transient absorption (TA) spectroscopy of (a) pristine ZIS nanosheets and (b) O-doped ZIS nanosheets. (c) Hydrogen-evolution rate of the O-doped ZIS nanosheets and pristine ZIS nanosheets. (d) Schematic illustration of the band structure of the O-doped ZIS and pristine ZIS samples. Reproduced with permission.[53] 2016, Wiley-VCH.

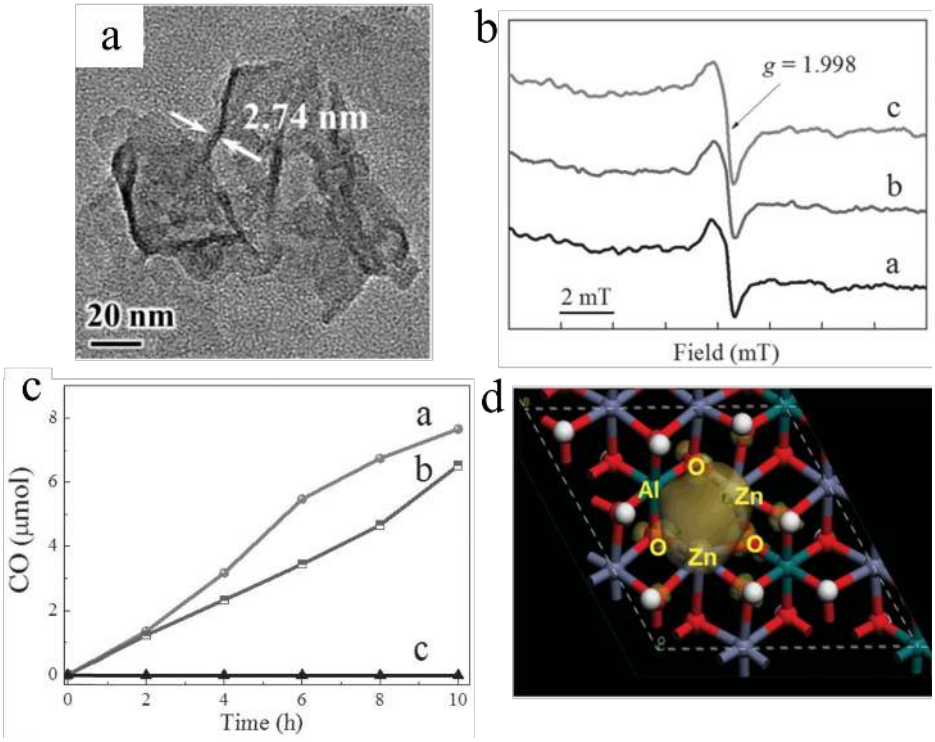

Figure 17. (a) TEM image and (b) ESR spectra of defect-rich ultrathin ZnAl-LDH, (c) time course of CO evolution in the photocatalytic conversion of CO_2 in the presence of water vapor under UV-vis light, (d) charge-density distribution for the valence band maximum of the defect-rich ultrathin ZnAl-LDH. Reproduced with permission.[43] 2015, Wiley-VCH.

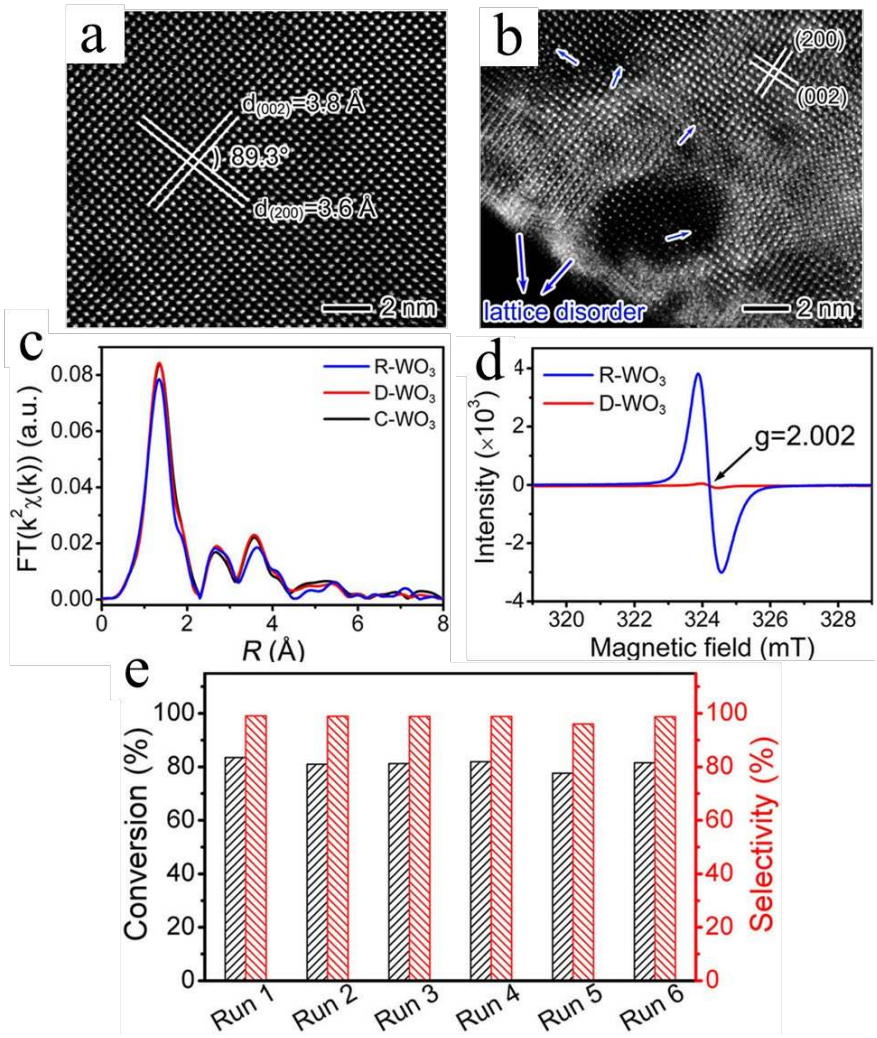

Figure 18. Atomic-resolution HAADF-STEM image of (a) defect-deficient WO_3 nanosheets and (b) defect-rich WO_3 nanosheets. (c) Fourier-transform W L_3-edge EXAFS spectra of the samples in reference to commercial WO_3, (d) Room-temperature ESR spectra, (e) cyclic test for defect-rich WO_3 in catalytic aerobic coupling of benzylamine under irradiation of $\lambda > 400$ nm at 298 K. Reproduced with permission.[128] 2016, American Chemical Society.

Table 1. Recent studies on ultrathin 2D materials for photocatalytic applications.

Photocatalysts	Thickness	Band structure	Reaction conditions	Photocatalytic efficiencies	Ref.
Pore-rich WO_3	3.8 nm	band gap 2.89 eV, CB -0.40 eV, VB 2.48 eV	1 mg sample coated on ITO, 0.5 mol L^{-1} Na_2SO_4 solution, applied potentials between 0 and 1.4 V versus Ag/AgCl, 300 W Xe lamp	Photocurrent density of 2.14 mA cm^{-2} at 1.0 V towards water oxidation	27
O-vacancies-rich In_2O_3	0.9 nm	band gap 2.18 eV	2.5 mg sample coated on ITO, 1 M KOH electrolyte, applied potentials -0.5 to +0.6 V vs. Ag/AgCl, 300 W Xe lamp with 420 cut-off filter	Photocurrent density of 1.73 mA cm^{-2} at 0.576 V towards water oxidation	34
NiTi-LDH	~2 nm	band gap 2.1 eV	50 mg sample dispersed in 50 mL 0.01 M $AgNO_3$, 300 W Xe lamp with 400 cut-off filter	~2148 μmol g^{-1} h^{-1} for O_2 evolution	45
SnS	0.57 nm	band gap 1.47 eV	0.5 mol L^{-1} Na_2SO_4 solution, applied potentials -0.4 to +0.8 V vs. Ag/AgCl, 300 W Xe lamp with 420 cut-off filter	Photocurrent density of 5.27 mA cm^{-2} at 0.8 V towards water oxidation	50
SnS_2	0.61 nm	band gap 2.23 eV	1.5 mg sample coated on ITO, 0.5 mol L^{-1} Na_2SO_4 solution, applied potentials -0.45 to +1.0 V vs. Ag/AgCl, 300 W Xe lamp with 420 cut-off filter	Photocurrent density of 2.75 mA cm^{-2} at 1.0 V towards water oxidation	51
Co-doped In_2S_3	0.59 nm	—	2.5 mg sample coated on ITO, 1 M KOH electrolyte, applied potentials 0 to +0.5 V vs. Ag/AgCl, 300 W Xe lamp with 420 cut-off filter	Photocurrent density of 1.17 mA cm^{-2} at 0.476 V towards water oxidation	52
ZnSe	0.85 nm	band gap 3.5 eV	1.5 mg sample coated on ITO, 0.5 mol L^{-1} Na_2SO_4 solution, applied potentials -0.4 to +0.8 V vs. Ag/AgCl, 300 W Xe lamp	Photocurrent density of 2.14 mA cm^{-2} at 0.72 V towards water oxidation	55
Cu_2O	0.62 nm	band gap 1.92 eV	5 mg sample coated on ITO, 0.5 mol L^{-1} Na_2SO_4 solution, applied potentials -1.0 to -0.6 V vs. Ag/AgCl, 300 W Xe lamp with 420 cut-off filter	Photocurrent density of 3.98 mA cm^{-2} at -1.0 V towards hydrogen evolution	31
HNb_3O_8	1.3 nm	band gap 3.68 eV	100 mg HNb_3O_8 dispersed in 100 mL of a 10% TEOA solution, 1% Pt, 125 W Hg lamp	ca. 61 μmol h^{-1} for hydrogen evolution	35
$HNbWO_6$	1.8-2.0 nm	band gap 3.13 eV, CB -0.68 eV, VB 2.45 eV	80.0 mL $HNbWO_6$ nanosheets dispersion, triethanolamine solution, 1 wt% Pt, 300 W Xe lamp	158.9 μmol h^{-1} for hydrogen evolution	39
$SnNb_2O_6$	~3 nm	band gap 2.43 eV	50 mg sample dispersed in 20 mL 20 vol% lactic acid solution, 0.3 wt% Pt, 300 W Xe lamp with 400 cut-off filter	13.2 μmol h^{-1} for hydrogen evolution	40

CoOOH	1.5 nm	band gap 2.4 eV	8 mg sample dispersed in 100 mL 0.5 M Na_2SO_3, 300 W Xe lamp	1200 μmol g^{-1} h^{-1} for hydrogen evolution	44
CdS	~4 nm	band gap ~2.86 eV	1.425 mg sample dispersed in 30 mL 0.25 M Na_2S and 0.25 M Na_2SO_3 solution, 300 W Xe lamp with 420 cut-off filter	41.1 mmol h^{-1} g^{-1} for hydrogen evolution	47
O-doped $ZnIn_2S_4$	6 nm	band gap 2.07 eV, CB -1.34 eV, VB 0.73 eV	20 mg sample dispersed in 200 mL 0.25 M Na_2SO_3 and 0.35 M Na_2S solution, 300 W Xe lamp with 420 cut-off filter	2120 μmol g^{-1} h^{-1} for hydrogen evolution	53
Fe-BiOCl	3.7 nm	band gap 2.65 eV, CB -1.05 eV, VB 1.60 eV	25 mg sample dispersed in 50 mL 0.1 M Na_2SO_4, 300 W Xe lamp with 420 cut-off filter	3.54 μmol h^{-1} for hydrogen evolution	68
g-C_3N_4	~2 nm	band gap 2.97 eV	50 mg sample dispersed in 300 mL 10 vol% triethanolamine solution, 6 wt% Pt, 300 W Xe lamp	170.5 μmol h^{-1} for hydrogen evolution	69
O-g-C_3N_4	~0.64 nm	band gap 2.85 eV, CB -1.06 eV, VB 1.79 eV	50 mg sample dispersed in 100 mL 10 vol% triethanolamine solution, 3 wt% Pt, 300 W Xe lamp with 400 cut-off filter	~8874.7μmol g^{-1} h^{-1} for hydrogen evolution	73
g-C_3N_4	~2 nm	band gap 2.65 eV	50 mg sample dispersed in 100 mL 10 vol% triethanolamine solution, 3 wt% Pt, 300 W Xe lamp with 420 cut-off filter	93 μmol h^{-1} for hydrogen evolution	75
Carbon nitride	~3.6 nm	band gap ~2.85 eV	50 mg sample dispersed in 100 mL 10 vol% methanol solution, 3 wt% Pt	53 μmol h^{-1} for hydrogen evolution	77
MoS_2/$Bi_{12}O_{17}Cl_2$	0.71 nm of $Bi_{12}O_{17}Cl_2$	band gap ~2.5 eV	10 mg sample dispersed in 80 mL 0.3 M ascorbic acid solution, 300 W Xe lamp with 420 cut-off filter	33 mmol g^{-1} h^{-1} for hydrogen evolution	81
Rh-doped calcium niobate	~2.8-3.0 nm	band gap ~1.9 eV	5 mg sample dispersed in 150 mL 10 vol% methanol solution, 500 W Xe lamp	384.8 μmol h^{-1} for hydrogen evolution	86
C-BN	3-4 nm	band gap 2.72 eV, CB -1.24 eV, VB 1.48 eV	50 mg sample dispersed in 100 mL 10 vol% triethanolamine solution, 1 wt% Pt, 300 W Xe lamp	ca. 46 μmol h^{-1} for hydrogen evolution	93
Rh single atoms/TiO_2	0.7 nm	—	20 vol% methanol solution, 500 W Xe lamp	51 μmol h^{-1} for hydrogen evolution	107
$MoSe_2$/$ZnIn_2S_4$	2.5 nm of $ZnIn_2S_4$	band gap ~2.75 eV	5 mg sample dispersed in 9 mL water and 1 mL lactic acid, 300 W Xe lamp with 400 cut-off filter	6,454 μmol g^{-1} h^{-1} for hydrogen evolution	120
TiO_2	1.66 nm	band gap ~3.2 eV	0.5 g sample dispersed in 140 mL water, high purity CO_2 gas was continuously bubbled, 300 W Hg lamp	1.9 μmol g^{-1} h^{-1} for CO_2 reduction to formate	24
Defect-rich ZnAl-LDH	~2.7 nm	band gap ~3.5 eV	100 mg sample, 100 mL CO_2, 0.4 mL H_2O, 300 W Xe lamp	7.6 μmol g^{-1} h^{-1} for CO_2 reduction to CO	43
Bi_2WO_6	1.65 nm	band gap 3.47 eV	0.2 g sample dispersed in 140 mL H_2O, high purity CO_2 gas was continuously bubbled, 300 W Xe lamp	75 μmol g^{-1} h^{-1} for CO_2 reduction to methanol	57
Phosphate and O-vacancy modified Bi_2WO_6	1.66 nm	band gap 2.06 eV	The catalyst was dispersed on a quartz cell in gas closed reaction system with distilled water and pure CO_2, 300 W Xe lamp with 400 cut-off filter	157 μmol g^{-1} h^{-1} for CO_2 reduction to methanol	58

V-vacancies-rich o-$BiVO_4$	1.28 nm	band gap 2.82 eV, CB -0.46 eV, VB 2.36 eV	0.2 g sample dispersed in 160 mL H_2O, high purity CO_2 gas was continuously bubbled, 300 W Xe lamp	398.3 μmol g^{-1} h^{-1} for CO_2 reduction to methanol	60
Zn-vacancies-rich $ZnIn_2S_4$	2.46 nm	band gap 2.58 eV	100 mg sample, 2 mL H_2O, filled with CO_2, 300 W Xe lamp	33.2μmol g^{-1} h^{-1} for CO_2 reduction to CO	123
MoS_2	3~5 layer	band gap 1.86 eV, CB -0.35 eV, VB 1.51 eV	15 mg sample dispersed in 200 mL H_2O, N_2 was continuously bubbled, 500 W Xe lamp with 420 cut-off filter	325 μmol g^{-1} h^{-1} for ammonia production	49
TiO_2	1-7 nm	band gap 3.14 eV	20 mg sample dispersed in 100 mL RhB solution (10 mg L^{-1}), UV radiation (wavelength peak at 365 nm)	4.3 times increased activity than P25 for RhB degradation	25
Bi_2WO_6	0.8 nm	band gap 2.7 eV	20 mg sample dispersed in 80 mL RhB solution (10 mg L^{-1}), 300 W Xe lamp with 420 cut-off filter	98% of RhB are degraded within 25 min	56
BiOCl	~2.7 nm	band gap 3.0 eV, CB -1.83 eV, VB 1.17 eV	5 mg sample dispersed in 100 mL RhB solution (10^{-5} M), 150 W Xe lamp	98% of RhB are degraded after 20 min	63
TiO-C_3N_4	3-3.3 nm	band gap 2.23 eV	50 mg sample dispersed in 100 mL RhB solution ($2*10^{-5}$ mol L^{-1})	RhB can be fully degraded within 10 min	110

Jun Di received his BS degree from the Jiangsu University in 2012. He is a PhD candidate under the tutelage of Professor Huaming Li at Jiangsu University and currently a Joint PhD candidate under the guidance of Assistant Professor Zheng Liu at Nanyang Technological University. His research interests focus on the design and synthesis of 2D materials for energy conversion.

Huaming Li received his BS degree from China West Normal University in 1985 and master degree from Chinese Academy of Sciences in 1992. At present, he is a full professor at the Jiangsu University. His current research is focused on nanomaterials, ionic liquids for energy and environmental applications.

Zheng Liu received his BSc (2005) from Nankai University and PhD (2010) in Physics from the National Center for Nanoscience and Technology (NCNST), China. He is Nanyang assistant professor at Nanyang Technological University. His research focus on the growth, characterizations, and performance of large-scale and high-quality novel low-dimensional crystals, including hexagonal boron nitride, metal dichalcogenides, and their hybridized architectures, as well as their applications on high-performance electronics, optical devices, and energy conversion and storage.

Recent progress in the research and development of ultrathin 2D photocatalysts is reviewed. Different strategies to tailor the electronic structures and hybridizations with the maintaining the ultrathin 2D structure are presented to further boost the photocatalytic activity. The advancement of versatile photocatalytic applications of ultrathin 2D photocatalysts are also discussed.

Keyword: ultrathin, two-dimensional, photocatalytic, electronic structure tailoring, hybridization

Jun Di[‡], Jun Xiong[‡], Huaming Li[*], Zheng Liu[*]

Ultrathin Two-dimensional Photocatalysts: Electronic Structure Tailoring, Hybridization and Applications

ToC figure